Advanced Photocatalytic Nanomaterials for Degrading Pollutants and Generating Fuels by Sunlight

Dieqing Zhang, Guisheng Li and Jimmy C. Yu

Abstract This chapter focuses on the recent development of sunlight-driven heterogeneous photocatalysts with different chemical compositions and nanostructures. Various photocatalytic nanomaterials, including metal oxides, heterojunction nanocomposites, oxynitrides, oxysulfides, and graphitic carbon nitride, are described. Their preparation methods as well as the mechanisms involved are introduced. These materials can be used to degrade pollutants and generate fuels. Photocatalytic evolution of H_2 from water and conversion of CO_2 to fuels are discussed in detail. The development of advanced photocatalytic technology involving novel nanomaterials may allow the construction of clean and facile systems for solving the global energy and environmental problems.

1 Introduction

Environment and energy are two of the world's most challenging issues. For a sustainable society, it is absolutely necessary to develop efficient pollution treatment technologies and harvest clean energy. Photocatalysis has a role to play in both aspects. Photocatalysis is a natural phenomenon that promotes chemical reactions on the surface of an irradiated semiconductor. The essence of the photocatalysis is attributed to the property of photo-excited carriers

D. Zhang · J. C. Yu (✉)
Department of Chemistry, Environmental Science Programme,
and Institute of Environment, Energy and Sustainability,
The Chinese University of Hong Kong, Shatin, New Territories,
Hong Kong, China
e-mail: jimyu@cuhk.edu.hk

D. Zhang · G. Li
Department of Chemistry, Shanghai Normal University, 200234 Shanghai, China
e-mail: lgscuhk@yahoo.com.cn

L. Zang (ed.), *Energy Efficiency and Renewable Energy Through Nanotechnology*,
Green Energy and Technology, DOI: 10.1007/978-0-85729-638-2_20,

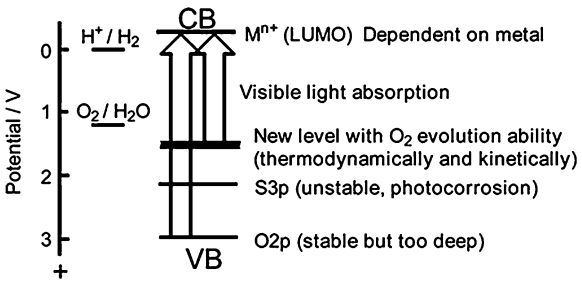

Fig. 1 Band structure control to develop visible-light-driven photocatalysts for water splitting. Reprinted with permission from Ref. [2]. Copyright 2009 American Chemical Society

(electrons and holes) with strong oxidization and reduction power. The redox reactions contribute to the decomposition of hazardous pollutants, conversion of carbon dioxide to valuable hydrocarbons, and the decomposition of water to hydrogen and oxygen.

Photocatalysts are materials that can realize the photocatalysis process. Much attention has been paid to these materials for the development of environment-friendly technology [1–9]. Titanium dioxide (TiO_2) is the most widely used photocatalyst. However, TiO_2 displays a high activity only when it is irradiated by UV light, where the light wavelength is shorter than 400 nm. It is therefore not efficient under sunlight irradiation. Suitable band engineering is required to develop new photocatalysts for solar applications (shown in Fig. 1) [2]. In this chapter, we discuss the fundamental issues that govern the design of visible-light responsive photocatalysts. We also describe some of their applications in environmental and energy aspects.

2 Solar-Light-Driven Photocatalysts for Degrading Pollutants

2.1 Doped TiO_2 Photocatalysts

The band gap of bulk TiO_2 lies in the UV regime (3.0 eV for the rutile phase and 3.2 eV for the anatase phase) [10]. Solar application of TiO_2 materials is limited by its wide band gap because pure TiO_2 can only absorb a small fraction of the sun's energy (<10%). To improve the efficiency, doping TiO_2 with metal/nonmetal atoms has proven an efficient route to broadening the photoresponse of TiO_2 to include the visible-light region. Recently, Chen et al. reviewed the modification of TiO_2 with metal/non-metal atoms in detail [10]. Herein, we will focus on the latest reported work related to doping metal/non-metal atoms into the TiO_2 framework.

2.1.1 Metal Doped TiO_2

A number of metal atoms have been doped into the framework of TiO_2 nanomaterials [11–17]. Besides the traditional methods, such as wet chemistry, high-temperature treatment, and ion implantation, various novel routes have been

developed for doping metal atoms into the TiO_2 nanomaterials. These include hydro-alcohol thermal, electrospinning, and flame spray pyrolysis (FSP) techniques. Yu et al. fabricated Fe-doped TiO_2 (Fe-TiO_2) nanorods with an impregnating-calcination method using a hydrothermally-prepared titanate nanotube as a precursor and $Fe(NO_3)_3$ as the dopant. Fe-doping greatly enhanced the visible-light photocatalytic activity of mesoporous TiO_2 nanorods, and when the atomic ratio of Fe/Ti (R-Fe) was in the range of 0.1–1.0%, the photocatalytic activity of the samples was higher than that of Degussa P25 and pure TiO_2 nanorods. At R-Fe = 0.5%, the photocatalytic activity of Fe-TiO_2 nanorods exceeded that of Degussa P25 by a factor of more than two [11]. Wang et al. prepared mesoporous W^{6+}-doped TiO_2 thin film photocatalysts by electrospinning and sol–gel chemistry through employing a triblock copolymer as a structure-directing agent. 3% W^{6+} was found to be the most suitable doping concentration, at which the recombination of photoinduced electrons and holes were effectively inhibited [12]. Li et al. fabricated V-doped TiO_2 (V-TiO_2) nanoparticles using a simple one-step FSP technique. Under visible-light irradiation, the degradation rate of 2, 4-dichlorophenol over 1% V-TiO_2 was two times higher than that of undoped TiO_2 [13]. Li et al. further utilized the one-step FSP technique to fabricate Cr-doped TiO_2 nanoparticles. The optimal Cr^{3+} concentration was found to be 1% [14]. Lorret et al. prepared nanocrystalline tungsten-doped titanium dioxide powders using a sol–gel method based on the hydrolysis of $TiCl_4$ in aqueous solution. Introducing tungsten into the TiO_2 framework could effectively extend light absorption of the TiO_2-based photocatalysts toward the visible-light range [15]. Dai et al. used a hydro-alcohol thermal method to fabricate Fe-doped titanium dioxide (TiO_2) microspheres with special core–shell structures. The concentration of Fe^{3+} played a key role in the photocatalytic degradation of phenol. Moreover, the 0.5 mol% Fe^{3+} doping was an optimal amount [16]. Yang et al. found that doping ruthenium, by an ion-exchange method, on the hydrothermally synthesized titania nanotube (Ti-NT) greatly enhanced the photocatalytic activity for degrading methylene blue (MB) dye under visible-light irradiation [17].

2.1.2 Non-Metal Doped TiO_2

Different nonmetal elements, such as B, C, N, F, and S, have been utilized recently to modify TiO_2 nanomaterials [18–26]. Xu et al. fabricated B-doped titania hollow spheres. They found that doping boron atoms effectively enhanced the photocatalytic activity of the hollow titania spheres in the degradation of Reactive Brilliant Red dye X-3B (C.I. Reactive Red 2) under-visible light irradiation [18]. Choi et al. reported a carbon-doped TiO_2 (C-TiO_2) photocatalyst prepared from a conventional sol–gel synthesis without using external carbon precursors. The carbon atoms from the titanium alkoxide precursor were incorporated into the lattice of TiO_2, creating mid-bandgap electronic states through controlled calcination [19]. Lu et al. demonstrated a facile route for the one-pot synthesis of visible-light responsive nitrogen-doped anatase TiO_2 sheets with dominant facets of TiN.

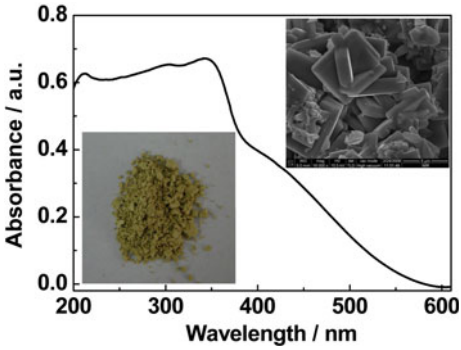

Fig. 2 UV–visible absorption spectra of (**a**) pure anatase TiO_2 sheets and (**b**) nitrogen-doped anatase TiO_2 sheets; the *insets* in the *upper right* and *lower left* corners are the plot of transformed Kubelka–Munk function vs the energy of light and optical photo of nitrogen-doped anatase TiO_2 sheets. Reprinted with permission from Ref. [27]. Copyright 2009 American Chemical Society

The as-synthesized anatase TiO_2 sheets showed a strong and stable ability to generate hydroxyl radicals [27].

The UV–visible absorption spectra of the anatase TiO_2 sheets (Fig. 2) shows an additional high visible-light absorption band from 400 nm to ca. 570 nm, consistent with the yellow color of the sample (see inset of Fig. 2). Derived from the plot of the Kubelka–Munk function versus the energy of the light absorbed, assuming titania is an indirect semiconductor, the bandgap of the obtained anatase TiO_2 sheets is extrapolated to be 3.11 eV, which is nearly identical to that of pure bulk anatase TiO_2. However, such nitrogen-doped {001}-dominant anatase TiO_2 sheets show a significantly enhanced visible-light absorption [27]. Yu et al. used a one-step low-temperature hydrothermal approach to fabricate hierarchical porous F-doped TiO_2 microspheres as shown in Fig. 3. These hierarchical porous microspheres exhibited high activity in the photocatalytic degradation of 4-chlorophenol under visible-light illumination [28].

Yu et al. proposed a one-step low-temperature hydrothermal route to synthesize S-doped TiO_2 photocatalysts from TiS_2 and HCl. Sulfur atoms could be efficiently doped into the anatase lattice under the mild hydrothermal conditions. The S-doped TiO_2 prepared by this hydrothermal approach exhibited much higher photocatalytic activity than that obtained by the traditional high-temperature thermal annealing method for the degradation of 4-chlorophenol under visible-light irradiation [29]. Li et al. prepared a S-doped TiO_2 by treating a TiO_2 xerogel under supercritical conditions in CS_2/ethanol fluid. The TiO_2 was modified through forming S–Ti–O bonds rather than adsorbing CS_2. During liquid-phase photocatalytic degradation of MB under visible-light irradiation, the S-doped TiO_2 exhibited higher activity than that of the undoped TiO_2 and even the N-doped TiO_2 obtained via supercritical treatment. A maximum activity of nearly eight times higher than that of commercially available Degussa P25 was obtained at a 1.8% S/Ti molar ratio [22].

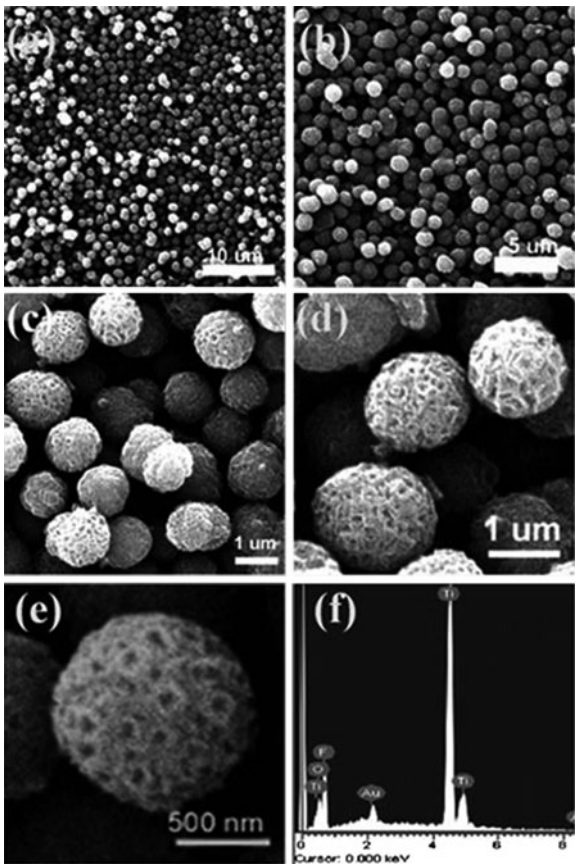

Fig. 3 SEM images of (**a**–**d**) porous F-doped TiO_2 microspheres with different magnifications; (**e**) an individual single microsphere showing detailed texture and porosity (ca. 1 μm in diameter); (**f**) EDX microanalysis spectrum of porous F-doped TiO_2 microspheres. Ref. [28]—reproduced by permission of The Royal Society of Chemistry

2.2 Nano-heterojunction (TiO_2-Based) Photocatalytic Materials

Modification of the TiO_2 band gap by doping [30–34] and development of new semiconductor materials capable of absorbing visible light [35] are the major strategies for developing visible-light photocatalysts. However, the low quantum efficiency, owing to the fast recombination of photo-generated electron–hole pairs, is still a challenge. This can be partially overcome by the construction of a heterojunction interface between semiconductors with matching band potentials. This allows electric-field-assisted charge transport from one particle to the other [36]. To date, the reported heterojunction semiconductors mainly fall into two categories: TiO_2-based photocatalysts [37, 38] and a small number of non-TiO_2-based systems [39, 40].

Recently, Yu et al. reported a cadmium sulfide quantum dots (QDs) sensitized mesoporous TiO_2 heterojunction photocatalyst [41]. It was prepared by preplanting cadmium oxide as crystal seeds into the framework of ordered mesoporous titanium dioxide and then converting CdO to CdS QDs through ion-exchange (as shown in Fig. 4).

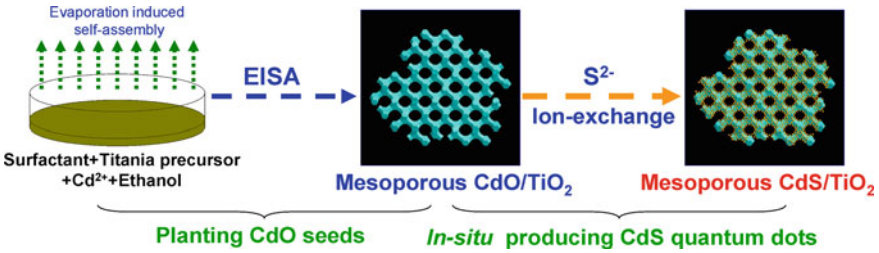

Fig. 4 Schematic synthesis route to ordered mesoporous CdS/TiO_2. Reprinted with permission from Ref. [41]. Copyright 2009 American Chemical Society

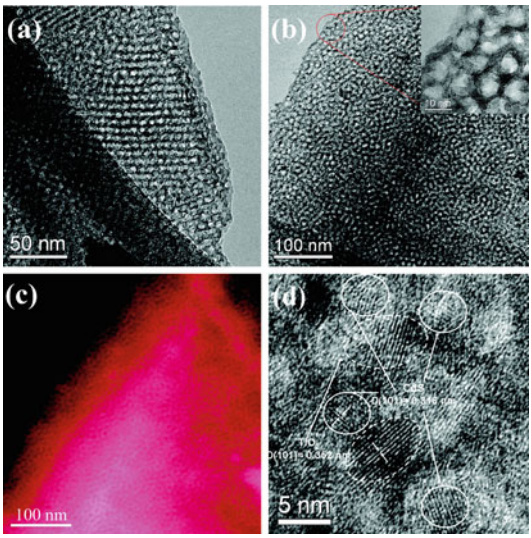

Fig. 5 **a** Standard TEM of CdO/TiO_2, **b** TEM image of CdS/TiO_2, **c** The chemical map of CdS/TiO_2 (*red areas* correspond to the S distribution) and **d** HRTEM image of CdS/TiO_2. Reprinted with permission from Ref. [41]. Copyright 2009 American Chemical Society

The presence of CdS QDs in the TiO_2 framework extended its photoresponse to the visible-light region by accelerating the photogenerated electron transfer from the inorganic sensitizer to TiO_2. The new photocatalyst showed excellent photocatalytic efficiency for both the oxidation of NO gas in air and the degradation of organic compounds (MB and 4-chlorophenol) in aqueous solution under visible-light irradiation [41]. As shown in Fig. 5a, the CdO/TiO_2 sample owned a long-range order structure. The ordered structure could be well maintained even after ion-exchange with S^{2-} (Fig. 5b), though distortions of the pore channels were observed, owing to the in situ transformation of CdO to CdS. The red areas in Fig. 5c represent the S distribution, and the black areas correspond to the pores of the mesoporous CdS/TiO_2. As illustrated in the map, virtually all CdS QDs are highly dispersed on the pore walls of the mesoporous TiO_2. This confirms that CdS QDs are well-integrated into the TiO_2 mesoporous network. The nanocrystalline nature of hexagonal CdS (solid ellipses) and anatase TiO_2 (dot ellipses) are well-

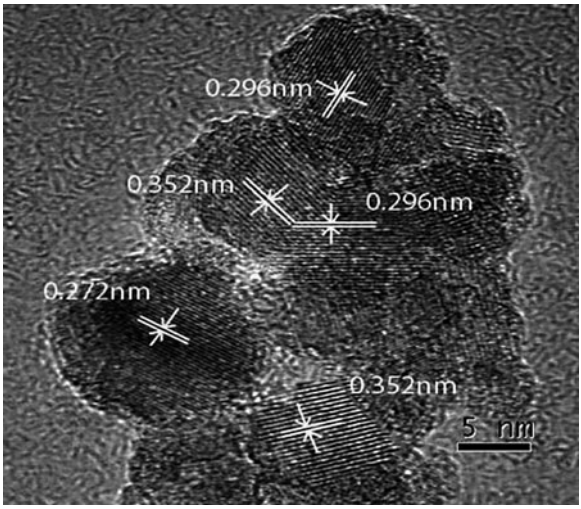

Fig. 6 High-resolution TEM image of $LaVO_4/TiO_2$ nanocomposite. Reprinted with permission from Ref. [43]. Copyright 2009 American Chemical Society

defined in the HRTEM image of CdS/TiO_2 as shown in Fig. 5d. These indicate that the heterojunction between CdS and TiO_2 were formed, owing to the intimate contact between CdS and TiO_2. These CdS/TiO_2 heterojunction will lead to a more efficient inter-electron transfer between the two components and improve the charge separation and, therefore, the photocatalytic activity [41, 42].

Li et al. fabricated $LaVO_4/TiO_2$ nanocomposite material with interconnected nanocrystal heterojunction by using a simple coupled method [43]. As shown in Fig. 6. The fringes of $d = 0.352$ nm matched the (101) crystallographic planes of anatase TiO_2, while the fringes of $d = 0.296$ nm and $d = 0.272$ nm matched the (012) and (202) crystallographic planes of monoclinic $LaVO_4$ nanoparticles. Meanwhile, interconnected fine nanoparticulate morphologies that confirmed the formation of $LaVO_4/TiO_2$ nanocrystal heterojunctions in the composite photocatalyst were observed [43].

This new type of heterojunction $LaVO_4/TiO_2$ nanocomposite exhibited very strong photocatalytic activity for decomposition of benzene under visible-light irradiation ($450 < \lambda < 900$ nm) with high photocatalytic stability. As shown in Fig. 7, the photocatalytic activities of T500, T400, P25, and $LaVO_4$ were very low under visible-light irradiation. Nevertheless, the $LaVO_4/TiO_2$ nanocomposite catalyst showed notably high visible-light photocatalytic activity [43]. Such enhanced photocatalytic performance of $LaVO_4/TiO_2$ can be attributed to the matched band potentials and the interconnected nanocrystal heterojunction of $LaVO_4$ and TiO_2. Figure 8 demonstrates a possible photocatalysis process for the degradation of benzene under visible-light irradiation. It includes four steps: (1) Upon visible-light irradiation, electrons and holes generated by $LaVO_4$ are separated. (2) Some electrons are injected into TiO_2 nanoparticles quickly because the conduction band (CB) of $LaVO_4$ is more negative than that of TiO_2. The formed nanostructure heterojunction on $LaVO_4/TiO_2$ composite can also lead to a more

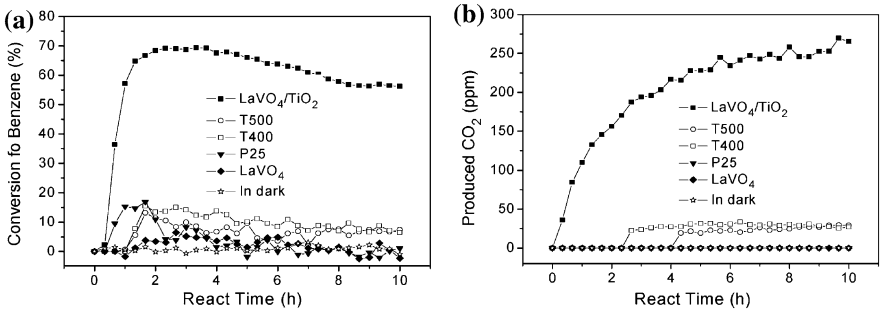

Fig. 7 Conversion of C_6H_6 (**a**) and the amount of produced CO_2 (**b**) on $LaVO_4/TiO_2$, T500, T400, P25, and $LaVO_4$ under visible-light irradiation and on $LaVO_4/TiO_2$ in the dark. Reprinted with permission from Ref. [43]. Copyright 2009 American Chemical Society

efficient inter-electron transfer between the two components [42]. (3) The photogenerated electrons are then captured by O_2 to yield O_2•- and H_2O_2, and then the OHo can be formed by reacting O_2•- with H_2O_2 [32]. The OH• owns a high ability to attack any organic molecules. (4) The photogenerated hole in $LaVO_4$ also may serve as oxidants to activate some unsaturated organic pollutants (e.g., benzene), leading to subsequent decomposition [43]. Since then, Li et al. reported a $Pb(Zr_{0.52}Ti_{0.48})O_3/TiO_2$ (PZT/TiO_2) composite photocatalyst with nanostructured heterojunction prepared by a simple sol–gel method. The as-prepared PZT/TiO_2 photocatalyst with large special surface area exhibited enhanced visible-light absorption and high efficient photocatalytic activity for decomposition of ethylene under visible-light irradiation with high photochemical stability [44].

A $FeTiO_3/TiO_2$ heterojunction structure containing a $FeTiO_3$ nanodisc and Degussa P25 was prepared by using maleic acid as an organic linker [45]. The $FeTiO_3$ nanodisc was a single-crystalline ilmenite phase with its face oriented in (001) plane and grown to the (110) direction. The 5/95 $FeTiO_3/TiO_2$ exhibited the optimized photocatalytic activity in removing 2-propanol and evolving CO_2 in the gas phase under visible-light irradiation. Its degradation constant (k) for removing 2-propanol was 25 times that of Degussa P25. The remarkably enhanced photocatalytic activity of $FeTiO_3/TiO_2$ was attributed to the intersemiconductor hole-transfer mechanism due to the unique relative band positions of these two semiconductors [45]. As shown in Fig. 9, the $FeTiO_3/TiO_2$ system is an example of the type-B heterojunction. The photocatalytic reaction takes place based on inter-semiconductor hole-transfer . The valence band (VB) position of $FeTiO_3$ is very close to that of TiO_2, while its CB is much lower than that of TiO_2 ($\sim$0.5 V lower). The VB of $FeTiO_3$ is rendered partially vacant by band gap excitation under visible-light irradiation. The electrons in the VB of TiO_2 can be transferred to that of $FeTiO_3$. Thus, the holes generated in VB of TiO_2 have a sufficient lifetime to initiate the various photocatalytic oxidation reactions [45].

FeOOH/TiO_2, a heterojunction structure between FeOOH and TiO_2, was prepared by covering the surface of the similar to 100-nm-sized FeOOH particles with

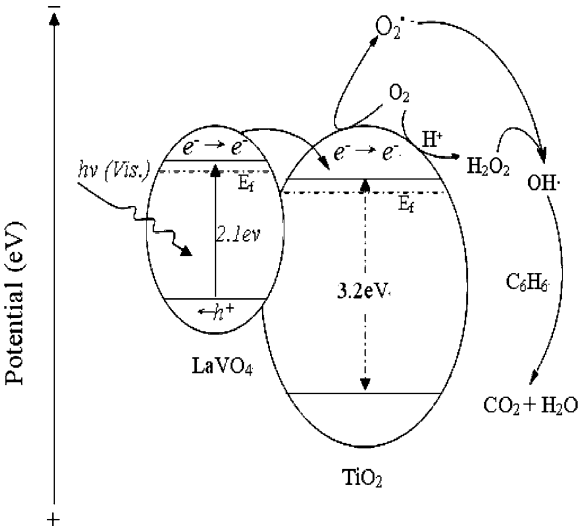

Fig. 8 Proposed mechanism for the visible-light photodegradation of benzene on $LaVO_4/TiO_2$ nanocomposite. Reprinted with permission from Ref. [43]. Copyright 2009 American Chemical Society

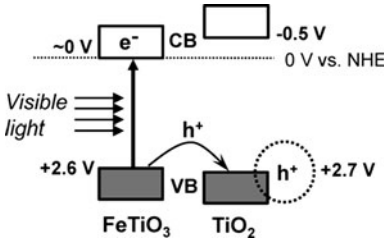

Fig. 9 Energy-band diagram illustrating the type-B heterojunction of TiO_2 and $FeTiO_3$ with visible-light irradiation. Reprinted with permission from Ref. [45]. Copyright 2009 American Chemical Society

Degussa P25 by applying maleic acid as ail organic linker [46]. Under visible-light irradiation, such $FeOOH/TiO_2$ heterojunction structure showed notable photocatalytic activity for the removal of gaseous 2-propanol and evolution of CO_2.

2.3 Non-TiO_2 Photocatalytic Materials

2.3.1 Bi_2WO_6

Semiconducting materials of the Aurivillius oxides $Bi_2A_{n-1}B_nO_{3n+3}$ (A = Ca, Sr, Ba, Pb, Na, K, and B = Ti, Nb, Ta, Mo, W, Fe) have been extensively studied because of their layer structure and unique properties [47, 48]. Among these compounds, Bi_2WO_6, as the simplest member of the Aurivillius family of layered perovskites, has been extensively utilized as an excellent photocatalyst for water splitting and photodegradation of organic compounds under visible-light irradiation [49–51]. Kudo et al. found that Bi_2WO_6 had photocatalytic activity for O_2 evolution [52] and Zou et al. revealed that Bi_2WO_6 could degrade organic compounds under visible-light irradiation [53]. Wang et al. fabricated flower-like

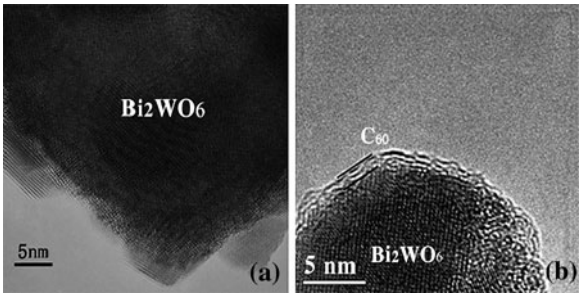

Fig. 10 HRTEM images of (**a**) Bi_2WO_6 and (**b**) the C_{60}-modified Bi_2WO_6 sample. Reprinted with permission from Ref. [57]. Copyright 2007 American Chemical Society

structured Bi_2WO_6 through the hydrothermal route without using any surfactants or templates. The products exhibited strong visible-light-driven photocatalytic performance for the treatment of RhB due to the novel hierarchical transport pores of the flower-like superstructures [54]. Subsequently, Xie et al. used the hydrothermal method to synthesize a Bi_2WO_6 hierarchical nest-like structure with the assistance of PVP [55]. Since then, new types of Bi_2WO_6 with complex morphologies, namely, flower-like, tyre- and helix-like, and plate-like shapes, were selectively synthesized via a hydrothermal process with P123 as a template by Wang et al. [56].

Recently, Zhu et al. prepared fullerene (C_{60}) modified Bi_2WO_6 photocatalyst by an absorbing process [57]. As shown in Fig. 10, the lattice structure of Bi_2WO_6 was observed from the center to the boundary (Fig. 10a). The outer boundary of Bi_2WO_6, modified by C_{60}, was distinctly different (Fig. 10b). An outer layer with an amorphous structure surrounded the surface of the Bi_2WO_6 nanosheet. The thickness of the layer was estimated to be about 1 nm, very close to the diameter of C_{60}. Therefore, it was concluded that C_{60} was dispersed on the surface of Bi_2WO_6 with a monolayer structure [57].

Such new composite photocatalyst exhibited a high efficiency for the degradation of nonbiodegradable azodyes MB and rhodamine B (RhB) under visible-light ($\lambda > 420$ nm) and simulated solar light ($\lambda > 290$ nm). The enhanced photocatalytic activity for the C_{60}-modified Bi_2WO_6 could come from the high migration efficiency of the photo-induced electrons on the interface of the C_{60} and Bi_2WO_6. The delocalized conjugated π structure of C_{60} made the transfer of photoinduced electrons easier [58]. The schematic of photocatalytic mechanism is shown in Fig. 11 [57].

More recently, Zhu et al. used a two-step process to synthesize F-substituted Bi_2WO_6 ($Bi_2WO_{6-X}F_{2X}$) photocatalysts with high activity. F-substitution changed the original coordination around the W and Bi atoms. Compared with Bi_2WO_6, the photocatalytic activity of $Bi_2WO_{6-X}F_{2X}$ increased about two times for the degradation of MB under visible light irradiation. Density functional calculations revealed that $Bi_2WO_{6-X}F_{2X}$ has a wider valence bandwidth and lower VB position. The high activities of $Bi_2WO_{6-X}F_{2X}$ photocatalysts come from its VB, which increase the mobility of photo-excited charge carriers and possess a stronger oxidation power [59].

Fig. 11 Possible pathway of the photoelectron transfer excited by visible-light irradiation including photocatalytic process for C60-modified Bi_2WO_6. Reprinted with permission from Ref. [57]. Copyright 2007 American Chemical Society

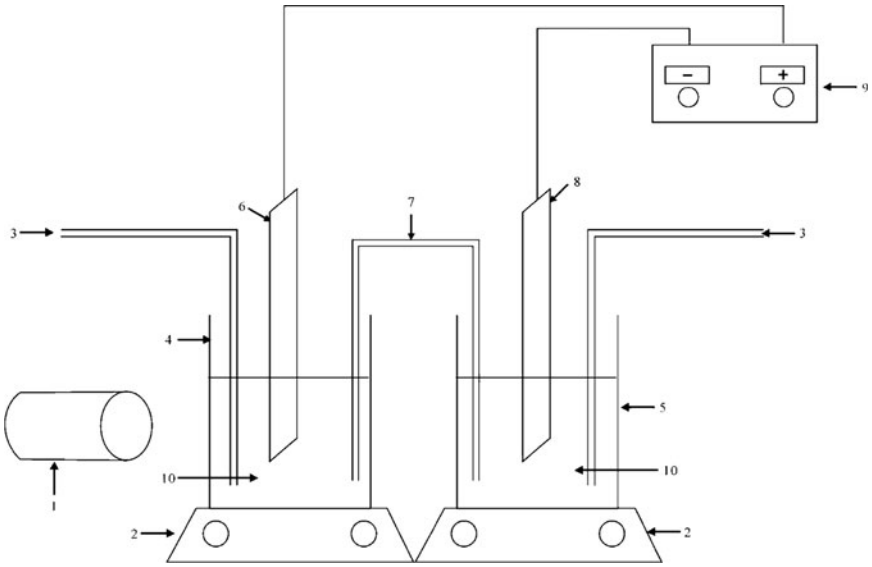

Fig. 12 Schematic illustration of a PEC system: (1) visible-light lamp; (2) magnetic stirrer; (3) air compressor; (4) anodic cell; (5) cathodal cell; (6) Bi_2WO_6/ITO electrode; (7) KCl bridge; (8) Pt cathode; (9) CHI-600A potentiostat; (10) RhB solutions. Reprinted with permission from Ref. [60]. Copyright 2007 American Chemical Society

Lin et al. introduced the photoelectrochemical (PEC) concept to the photocatalytic oxidation application of Bi_2WO_6 [60]. Hydrothermal combined with a spin coating technique was utilized to fabricate a Bi_2WO_6 nanoplate film electrode. As shown in Fig. 12, PCE experiments were performed in the anodic cell, using Bi_2WO_6/ITO electrode with the area of 3 cm^2 in 0.005 mol L^{-1} of Na_2SO_4 electrolyte solution under visible-light illumination. The voltage applied in the EC and PEC systems was 1.2 V. During the entire experiment, the solutions in the anodic and cathodal cells were magnetically stirred. During photocatalytic oxidation process, the Bi_2WO_6/ITO electrode only worked as a photocatalyst without an applied bias [60]. The PEC system based on Bi_2WO_6 nanoplate film electrode degraded 87.2% of RhB with concentration of 5 mg L^{-1} in 120 min, operated at low voltage and under visible-light irradiation, whereas only 36.8 and 39.5%

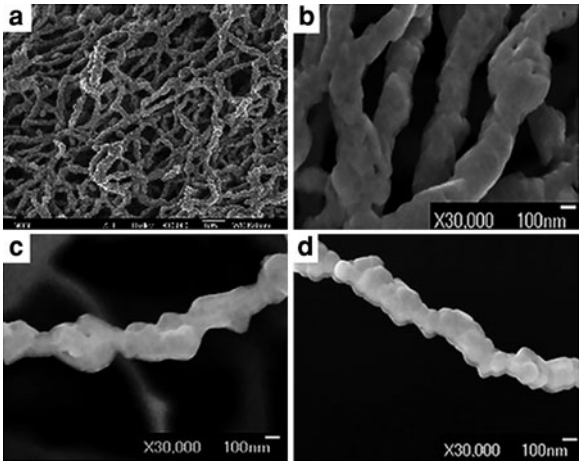

Fig. 13 The SEM images of Bi_2WO_6 nanofibers with (**a**) $R = 0.5$, (**b**) $R = 1$, (**c**) $R = 1.5$, and (**d**) $R = 2$. Ref. [61]—reproduced by permission of The Royal Society of Chemistry

degradation of RhB were observed for the electro-oxidation process (EC) and photocatalytic oxidation processes (PC), respectively, operated under the same condition. These results revealed a significant synergetic effect on degrading RhB via electro-oxidation and photocatalysis under visible-light irradiation [60].

Wang et al. developed an electrospinning technique to fabricate Bi_2WO_6 nanofibrous mat with excellent photoactivity under visible-light irradiation [61]. The as-prepared nanofibers are made of single-crystalline Bi_2WO_6 nanoparticles about 100 nm in size. The diameters of the nanofibers can be controlled by tuning the weight ratio (R) of Bi_2WO_6 to poly(vinyl pyrrolidone) (PVP). As shown in Fig. 13, when the R is 0.5 (Fig. 13a), it was unfavorable for the formation of uniform nanofibers, presumably due to the low content of Bi_2WO_6 nanoparticles that could not be connected during the calcination process. The average diameter of the Bi_2WO_6 nanofibers was about 450 nm. By increasing R from 1 to 2, the average diameter of the fibers decreased from 300 to 170 nm (Fig. 13b–d) [61]. In addition to the favorable recycling characteristics, the mat with $R = 2$ exhibited higher photocatalytic activity in the decomposition of acetaldehyde (CH_3CHO) and aqueous ammonia than that of the sample prepared by the solid-state reaction (SSR) and the nanoparticles. Electrospinning is favorable for the effective improvement of the photocatalytic activity of catalysts. It also can provide a solution to the separation problem in conventional catalysts that are small in size. Thus, it is worth considering for the preparation of other photocatalysts [61].

2.3.2 $BiVO_4$

$BiVO_4$, with a narrower band gap of 2.4 eV, is an important visible-light responsive photocatalyst, widely used in the evolution of photocatalytic O_2 and the photocatalytic degradation of organic pollutants [62, 63]. There are three naturally occurring crystal forms of $BiVO_4$, namely tetragonal zircon, monoclinic scheelite,

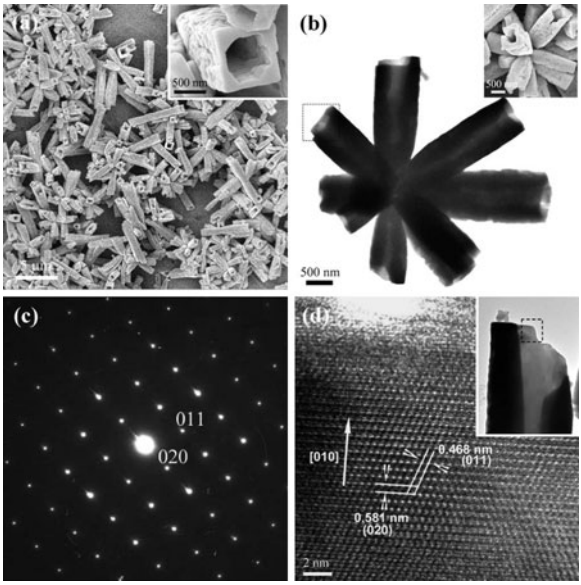

Fig. 14 $BiVO_4$ microtubes synthesized at 80°C for 6 h: **a** low-magnification SEM image of the product and high-magnification SEM image (*inset*) for a single $BiVO_4$ microtube, showing the hollow structure and wall thickness; **b** TEM and SEM image (*inset*) of an individual $BiVO_4$ microflower; **c** the corresponding SAED pattern taken from the rectangular part of the microtube in Fig. 14b; **d** HRTEM image near the nozzle of a single microtube (*inset*). Reprinted with permission from Ref. [68]. Copyright 2007 American Chemical Society

and tetragonal scheelite. Monoclinic scheelite presents the best photocatalytic performance under visible-light irradiation [64]. To date, various methods of synthesizing monoclinic scheelite $BiVO_4$ have been developed, including aqueous [62], solid-state [65], and hydrothermal processes [66], as well as organometallic decomposition [67].

Single-crystalline $BiVO_4$ microtubes, with novel square cross-sections and a flower-like morphology, were synthesized by a reflux method at 80°C [68]. The as-synthesized products were almost entirely microtubes with lengths of 2–5 μm. The individual tubes had well-defined square cross-sections with side lengths of ca. 800 nm and wall thicknesses of ca. 100 nm. The clear lattice fringe indicated the high-crystallinity and single-crystalline nature of the microtubes. The d spacings were found to be 0.581 and 0.468 nm, which agreed well with the lattice spacings of (020) and (011) of monoclinic $BiVO_4$ (Fig. 14c, d) [68]. The as-synthesized microtubes exhibited higher photocatalytic activity under visible-light radiation than that of the reference sample prepared by a solid-state reaction. This was ascribed to the special single-crystalline tubular structure and/or flower-like morphology [68].

Yu et al. used a nanocasting route to fabricate ordered mesoporous bismuth vanadate ($BiVO_4$) crystals using bismuth nitrate hydrate and ammonia meta-vanadate as bismuth and vanadium sources and silica (KIT-6) as a template [69]. Monoclinic scheelite $BiVO_4$ crystals were formed inside the mesopores of silica through a mild thermal process, and $BiVO_4$ was obtained after the removal of the hard template (silica) by NaOH treatment. Such product exhibited a superior photocatalytic performance in the photochemical degradation of MB and photocatalytic oxidation of NO gas in air under visible-light irradiation compared to

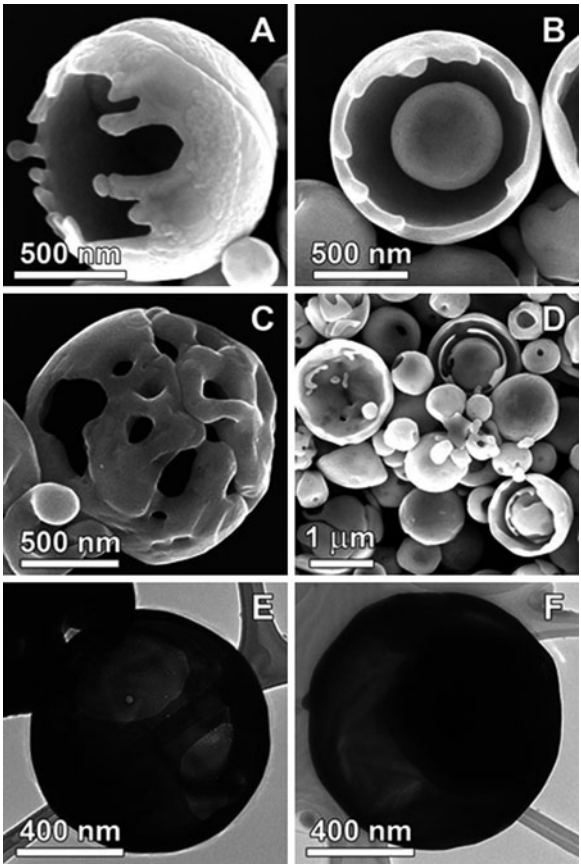

Fig. 15 **a–d** SEM and **e** and **f** TEM micrographs illustrating typical particle morphologies obtained during USP synthesis of $BiVO_4$. Reprinted with permission from Ref. [71]. Copyright 2009 American Chemical Society

conventional $BiVO_4$ [69]. Wang et al. used an aqueous strategy to synthesize two novel types of $BiVO_4$ mesocrystals with flower-like and dendrite morphology. The primary building units perfectly aligned in three-dimensions and built up well-defined mesocrystals with sharp facets and edges. The pH value and reaction temperature had great influences on the formation of these unique mesocrystals [70]. Recently, $BiVO_4$ powders with unique particle architectures were synthesized using ultrasonic spray pyrolysis (USP) [71]. These nanostructured $BiVO_4$ with particles range from thin, hollow, and porous shells to ball-in-ball type structures, as shown in Fig. 15. The $BiVO_4$ powders were utilized as an oxygen evolving photocatalyst and the kinetics of O_2 formation was studied in a $AgNO_3$ solution irradiated with $\lambda > 400$ nm light. USP prepared $BiVO_4$ was found to have superior photocatalytic activity compared to commercial $BiVO_4$ and WO_3, likely due to the differences in particle morphology [71].

Li et al. prepared a series of Cu-loaded $BiVO_4$ (Cu-$BiVO_4$) photocatalysts by the impregnation method [72]. The Cu-$BiVO_4$ series catalysts had significant optical absorption in the visible region between 550 and 800 nm and the

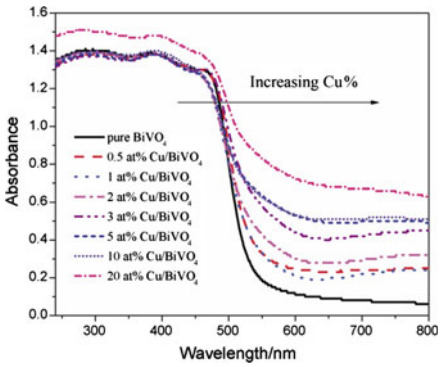

Fig. 16 UV–Vis diffuse-reflectance spectra of pure and Cu–$BiVO_4$ series catalysts. Reprinted from Xu et al. [72], copyright 2008 with permission from Elsevier

absorption intensity increased with the enhancement of Cu content as shown in Fig. 16. The photocatalytic activities of Cu-$BiVO_4$ catalysts for the degradation of MB were found to depend largely on the Cu content and the calcination temperature. The optimum Cu loading and calcination temperature were found to be 5% and 300°C [72]. Novel Pt/$BiVO_4$ composite photocatalysts with visible-light activities were prepared by the impregnation method [73]. Monoclinic scheelite structures of $BiVO_4$ were retained after the Pt species was doped. The visible-light absorption of the $BiVO_4$ photocatalysts was obviously enhanced upon modifying with Pt species (Fig. 17). The platinum doped in the composite photocatalyst was present in the form of platinum chloride ($PtCl_4$). The Pt species doping effectively enhanced the photoactivities of $BiVO_4$ samples in decomposition of methyl orange under visible-light irradiation [73].

2.3.3 Graphitic Carbon Nitrides (g-C_3N_4) Polymeric Photocatalyst

Among the different allotropes of carbon nitrides, the graphitic phase is usually regarded as the most stable under ambient conditions. Recently, graphitic carbon nitride (g-C_3N_4), as a conducting polymer semiconductor, has been proven an efficient photocatalyst for water splitting, even in the absence of noble metals [74]. Thermal polycondensation of common organic monomers was utilized to synthesize graphitic carbon nitrides (g-C_3N_4) with various architectures [75, 76]. As shown in Fig. 18, the graphitic planes are constructed from tri-s-triazine units connected by planar amino groups (Fig. 18a). Upon condensation at 823 K, an in-plane repeat period of 0.681 nm (for example, the distance between nitride pores) in the crystal is evident from the X-ray powder diffraction (XRD) pattern (Fig. 18b). It is smaller than one tri-s-triazine unit (0.713 nm), presumably owing to the presence of a small tilt angularity in the structure. The strongest XRD peak at 27.4, corresponding to 0.326 nm, is due to the stacking of the conjugated aromatic system. The band gap of the gold–yellow condensed graphitic carbon nitride is estimated to be 2.7 eV from its ultraviolet–visible spectrum (Fig. 18c). It implies an intrinsic semiconductor-like absorption in the blue region of the

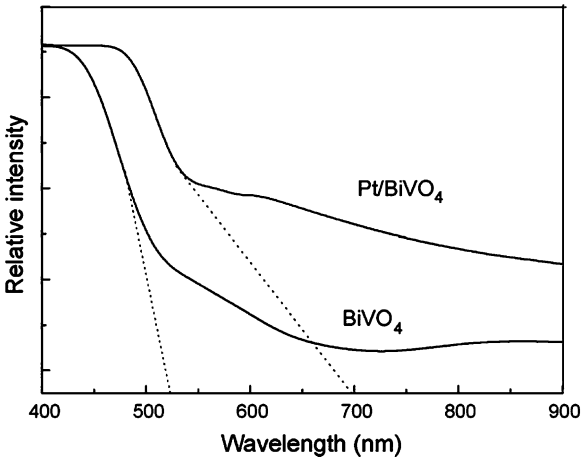

Fig. 17 UV–Vis diffuse absorption spectra of different photocatalysts. Reprinted from Ge [73], copyright 2008 with permission from Elsevier

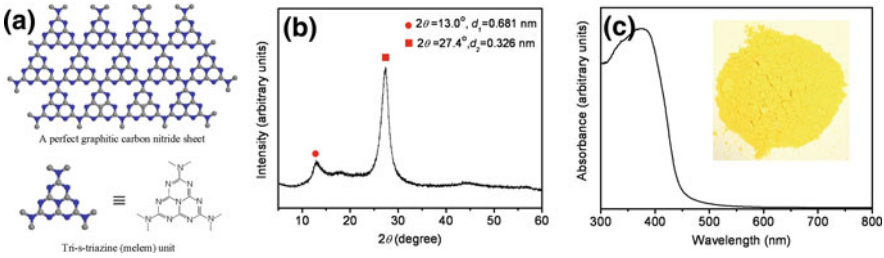

Fig. 18 Crystal structure and optical properties of graphitic carbon nitride. **a** Schematic diagram of a perfect graphitic carbon nitride sheet constructed from melem units. **b** Experimental XRD pattern of the polymeric carbon nitride, revealing a graphitic structure with an interplanar stacking distance of aromatic units of 0.326 nm. **c** Ultraviolet–visible diffuse-reflectance spectrum of the polymeric carbon nitride. *Inset*: Photograph of the photocatalyst. Reprinted by permission from Macmillan Publishers Ltd: (Nature Materials) (Ref. [74]), copyright 2009

visible spectrum. Such bandgap is sufficiently large to overcome the endothermic character of the water-splitting reaction (requiring 1.23 eV theoretically) [74].

Recently, the electronic and optical functions of polymeric g-C_3N_4 were further modified by the inclusion of metal species, such as Fe^{3+}, in its structure by a simple soft-chemical method without destroying the graphitic structure of the host. The metal components strongly affected the electronic properties of g-C_3N_4 and provided the material with additional new functionalities such as mimicking metalloenzymes in H_2O_2 activation. The metal species can significantly lower the bandgap and expand the light absorption of the material further into the visible region of the electromagnetic spectrum, while keeping a sufficient overpotential for carrying out oxidation reactions [77]. As shown in Fig. 19, the optical band gap energy gradually shifts to lower energies with increasing Fe content in the Fe/g-C_3N_4 hybrid materials. This suggests a host–guest interaction between

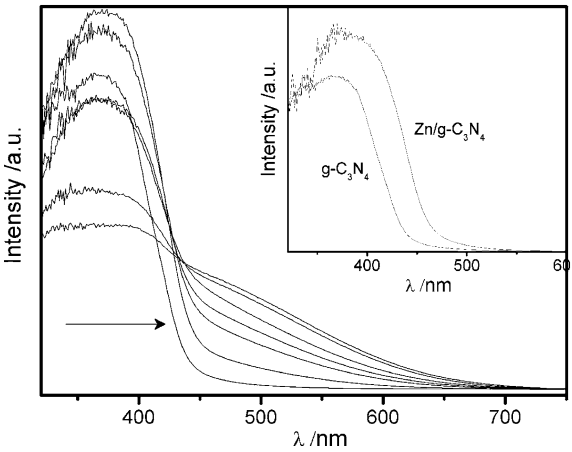

Fig. 19 Optical absorption spectra of Fe/g-C_3N_4 complexes and g-C_3N_4; the bandgap is shifted toward lower energies in the hybrid materials. Arrow direction: g-C_3N_4, 1%-, 3%-, 5%-, 10%-, 15%-, and 20%-Fe/g-C_3N_4. The *inset* is the optical spectrum of 10%-Zn/g-C_3N_4, which also demonstrates narrowing of the g-C_3N_4 bandgap by the metal inclusion. Wang et al. [77], copyright Wiley–VCH Verlag GmbH & Co. KGaA, reproduced with permission

g-C_3N_4 and the metal. A change in the optical absorption was also observed for Zn/g-C_3N_4 and is probably caused by the d–p repulsion of the Zn 3d and N2p orbitals [77, 78].

Photocatalytic experimental results confirmed that various organic dyes (e.g., RhB, MB, methyl orange, and p-hydroxyazobenzene) were be degraded by using H_2O_2 and Fe/g-C_3N_4. The photocatalyst can also be recovered and reused [77]. Figure 20 shows the results from the RhB-oxidation and control experiments. The overall efficiency of the process can be enhanced by photoillumination ($\lambda > 420$ nm). Various intermediates, such as hydroxylated and de-ethylated, were observed during the oxidation of RhB by H_2O_2 activated with Fe/g-C_3N_4. These can be further decomposed to smaller organic molecules, eventually being mineralized to CO_2 [77].

More recently Fe/g-C_3N_4 was found to be capable of activating hydrogen peroxide for the direct oxidation of benzene to phenol in mild conditions. Fe-g-C_3N_4 is active for the direct oxidation of benzene to phenol using hydrogen peroxide. By taking advantage of the photocatalytic functions of g-C_3N_4, the yield of the phenol synthesis can be markedly improved [79]. Figure 21a shows the catalytic properties of graphitic carbon nitride. Figure 21b implies that it is able to adsorb and activate benzene chemically (Fig. 21b) and, thus, catalyzed not only Friedel–Crafts reactions of benzene but also phenol synthesis using benzene and CO_2 [75, 80].

2.3.4 Heterojunction of Non-TiO_2 Semiconductors

Much progress has been achieved in the development of TiO_2-based heterojunction photocatalytic systems. However, there is still need to develop highly active photocatalysts working under visible light in order to put this technology into practical applications. Recently, heterojunctions of non-TiO_2 semiconductors has become a hot topic in the photocatalytic research field.

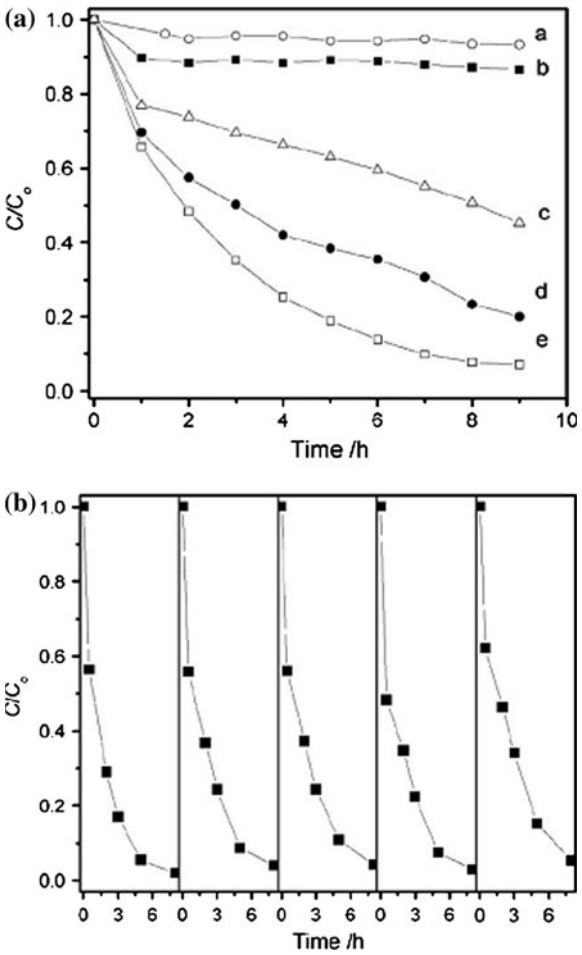

Fig. 20 **a** Concentration changes of RhB (10 mM) as a function of reaction time under different conditions: *a* H_2O_2 (0.01 M); *b* Fe/g-C_3N_4(40 mg); *c* Fe_2O_3(40 mg)/H_2O_2(0.01 M); *d* Fe/g-C_3N_4(40 mg)/H_2O_2(0.01 M); *e* Fe/g-C_3N_4(40 mg)/H_2O_2(0.01 M) under visible-light irradiation. **b** Cyclic runs of RhB (10 mM) degradation by H_2O_2 (0.05 M) activated by the Fe/g-C_3N_4 catalyst (40 mg). All reactions were carried out at neutral pH using the 10%-Fe/g-C_3N_4 catalyst. C: concentration; C_0: initial concentration. Wang et al. [77], copyright Wiley–VCH Verlag GmbH & Co. KGaA, reproduced with permission

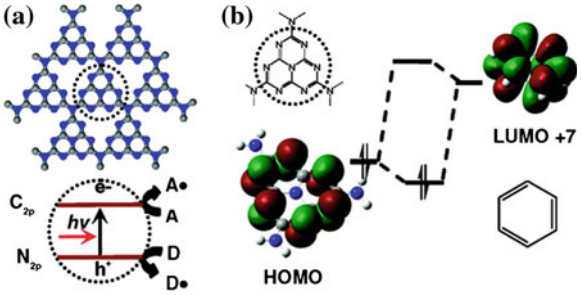

Fig. 21 **a** Stacked g-C_3N_4 sheets function as an all-organic solid-state photocatalyst promoting redox reactions with visible light. **b** Chemical interaction of benzene and defective g-C_3N_4 via HOMO–LUMO hybridization of melem and benzene. Reprinted with permission from Ref. [79]. Copyright 2009 American Chemical Society

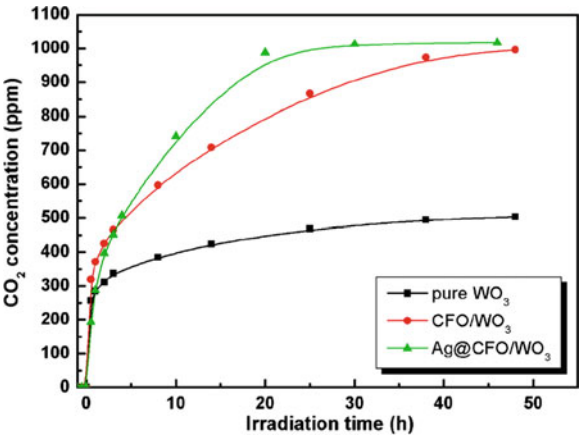

Fig. 22 CO_2 photogeneration profile at a long time visible irradiation. The initial acetaldehyde concentration is 500 ppm. The visible light density is 80 mW/cm^2. Reprinted with permission from Ref. [81]. Copyright 2009 American Chemical Society

Efficient visible-light active $CaFe_2O_4$ (CFO)/WO_3 composite photocatalysts were prepared by Miyauchi et al. [81]. The composite containing 5 wt% CFO showed optimized performance. Surface modification was made by heating the CFO/WO_3 composite or by coating the particle surface with Ag or ITO. The photocatalytic activity was greatly improved by coating the CFO particles with a Ag or ITO layer. The CO_2 generation profile over pure WO_3, 5 wt% CFO/WO_3, Ag@CFO/WO_3 photocatalysts were presented in Fig. 22. The CO_2 generation almost stops after 40 h of irradiation over pure WO_3. Pure WO_3 cannot completely decompose acetaldehyde to CO_2 even after more than 100 h under the present experimental conditions. However, acetaldehyde can be completely decomposed to CO_2 over a 5 wt% CFO/WO_3 composite in 48 h. It is impressive that the Ag modified composite Ag@CFO/WO_3 can reach complete decomposition of acetaldehyde in 20 h, which is more than twice as fast as the CFO/WO_3 photocatalysts [81].

A network-structured SnO_2/ZnO heterojunction nanocatalyst with high photocatalytic activity was synthesized through a simple two-step solvothermal method [82]. As shown in Fig. 23, the UV–vis absorption edges of the as-synthesized SnO_2 semicrystals and ZnO nanorods are located at about 305 and 380 nm, respectively. There are two prominent absorption bands for the SnO_2/ZnO sample. The former is assigned to the absorption of SnO_2 semicrystals and the latter is attributed to the characteristic absorption of ZnO nanocrystals. The absorption edges of SnO_2 and ZnO nanocrystals in the SnO_2/ZnO sample slightly shift toward blue. This indicates that the sizes of SnO_2 and ZnO in the SnO_2/ZnO sample are smaller than the corresponding values of pure SnO_2 or ZnO [82].

The photocatalytic activity of SnO_2/ZnO heterojunction nanocatalysts for the degradation of methyl orange is much higher than those of solvothermally synthesized SnO_2 and ZnO samples. Figure 24 shows the proposed band structure of the as-synthesized SnO_2/ZnO heterojunction nanocatalyst [82, 83]. Upon formation of the heterojunction between SnO_2 and ZnO, the different work functions will induce the negatively charged carriers to move from SnO_2 (the material with low

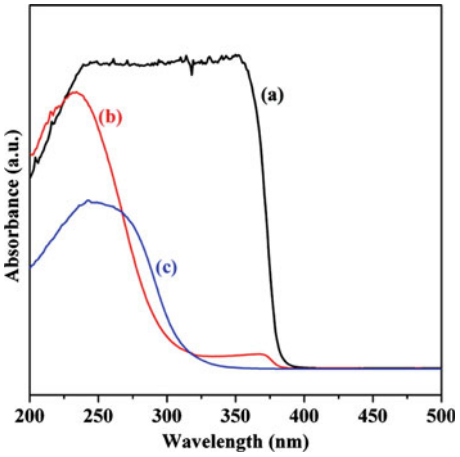

Fig. 23 UV–vis diffuse-reflectance spectra of the as-synthesized samples: (a) ZnO, (b) SnO_2/ZnO, and (c) SnO_2. Reprinted with permission from Ref. [82]. Copyright 2009 American Chemical Society

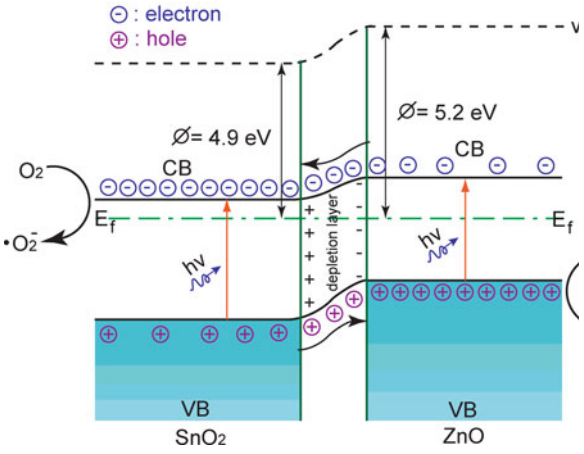

Fig. 24 Energy-band diagram and photocatalytic mechanism of the as-synthesized SnO_2/ZnO heterojunction nanocatalyst, where vac is the vacuum level, E_f is the Fermi level, CB is the conduction band, and VB is the valence band. Reprinted with permission from Ref. [82]. Copyright 2009 American Chemical Society

work function) to ZnO (the one with high work function) until their Fermi levels align (i.e., the system reaches thermal equilibrium). Thus, an electrostatic field is created at the interface. At thermal equilibrium, the CBs and VBs of SnO_2 and ZnO bend, and a depletion layer forms around the interface, too. Under UV light irradiation, electrons (e−) in the VB can be excited to the CB while simultaneously generating the same amount of holes (h+) in the VB. The photogenerated electrons and holes can be separated under the influence of the electrostatic field induced by different work functions. Therefore, electrons move to the SnO_2 side and holes to the ZnO side. The photogenerated electrons and holes in the SnO_2/ZnO heterojunction nanocatalyst can be injected into a reaction medium and participate in chemical reactions [82].

Bi_2O_3 is a good n-type semiconductor and $BaTiO_3$ is a high dielectric and ferroelectric material, where some atoms in the lattice are movable. Based on this, Huang et al. used a milling-annealing technique to prepare a heterojunction

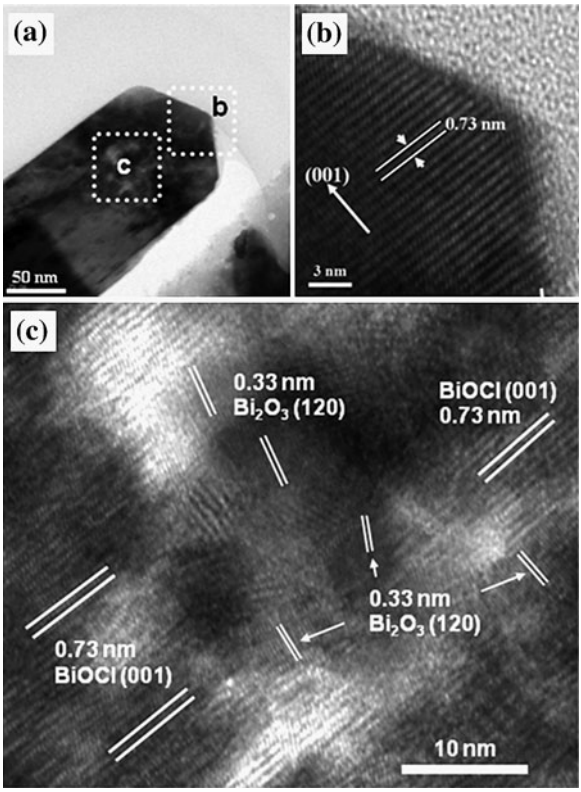

Fig. 25 TEM images for an 85/15 $BiOCl/Bi_2O_3$ particle. Typical TEM image (**a**), and HRTEM images for the outer (**b**) and inner (**c**) parts of the sample. Reprinted from Chai [35], copyright 2009 with permission from Elsevier

photocatalyst, $Bi_2O_3/BaTiO_3$ [36]. This technique has an advantage over the direct mixing method because it can construct a tight chemically bonded interface between the coupled materials. The heterojunction semiconductors $Bi_2O_3/BaTiO_3$ showed better photocatalytic activities than single-phase $BaTiO_3$ or Bi_2O_3 for degrading methyl orange and MB. The remarkable enhancement in the photocatalytic performance of $Bi_2O_3/BaTiO_3$ was ascribed mainly to the electric field-driven electron–hole separation at the interface and in the two semiconductors. Besides, the fair mobility for electron and hole transportation in Bi_2O_3 and $BaTiO_3$, respectively, were also favorable for the high photocatalytic property [36].

Lee et al. also reported a novel $BiOCl/Bi_2O_3$ heterojunction-type photocatalyst [35]. The TEM image in Fig. 25a reveals that the 85/15 $BiOCl/Bi_2O_3$ is a well-defined longish particle of $\sim$200 nm width. As shown in the high-resolution TEM image of Fig. 25b, the outer part of the $BiOCl/Bi_2O_3$ particle reveals a clear image, suggesting the presence of crystalline BiOCl. The uniform fringe, with an interval of 0.73 nm, is in good agreement with the (001) lattice plane of the tetragonal BiOCl. On the other hand, as shown in Fig. 25c, the TEM image for the core of the $BiOCl/Bi_2O_3$ particle is not as clear as that of outer part and several sets of mixed fringes are found, indicating the presence of mixed phases of BiOCl and Bi_2O_3 that is, the interlayer distance of 0.73 nm corresponds to the (001) lattice plane of BiOCl,

and that of 0.33 nm is consistent with the (120) plane of α-Bi_2O_3. These observations indicate that the nano-sized Bi_2O_3 grains are embedded here and there inside the BiOCl matrix [35]. Though both the individual BiOCl and Bi_2O_3 show very low photocatalytic efficiency under visible-light irradiation, their heterojunctions provide unexpectedly high efficiency in decomposing organic compounds. The BiOCl/Bi_2O_3 can induce complete mineralization without formation of intermediate species by utilizing the holes generated in the VB of BiOCl. Compared to the Degussa P25, it demonstrates 5.7 times the efficiency in evolving CO_2 from gaseous 2-propanol (IP) and 10.5 times the efficiency in removing aqueous 1, 4-terephthalic acid (TA) under visible-light irradiation. In this BiOCl/Bi_2O_3 system, the BiOCl seems to work as the main photocatalyst, while the role of Bi_2O_3 is a sensitizer, absorbing visible light [35].

3 Solar-Light-Driven Photocatalysts for Generating Fuels

3.1 Solar-Light-Driven Photocatalysts for H_2 Evolution

The concern for the depletion of fossil fuels and the environmental problems accompanying their use fostered the research for viable alternatives. Many research efforts have been devoted to the generation of hydrogen since it is the fuel with the highest energy capacity per unit mass. Hydrogen is also a clean energy carrier because it produces neither CO_2 nor pollutants. Many reviews on photocatalytic water splitting have been published [2, 9, 84–89]. In the following sections, we focus on visible-light-driven heterogeneous photocatalytic materials, such as metal oxides, metal oxynitrides, metal oxysulfides, metal sulfides, and polymers for H_2 evolution.

3.1.1 Metal Oxide Photocatalysts

To obtain photocatalytic activity under visible-light irradiation, it is essential to control the interdependence between the electronic, microstructural, and surface properties of photocatalysts by means of a careful design of both bulk and surface properties. The strategies can be classified in five categories: (a) developing new single-phase photocatalysts; (b) tuning the band gap energy with ion doping; (c) surface modification by depositing co-catalysts; (d) sensitization; and (e) controlling the defects, size, and morphology. This section briefly reviews the recent developments in oxide photocatalysts (Table 1) that show activity under visible light.

3.1.2 Oxynitride and Oxysulfide Photocatalysts

Domen and co-workers have done extensive studies on oxynitride and oxysulfide visible-light-driven photocatalysts [87, 88, 90–99]. The hydrogen generation application for these catalysts has been reviewed in previous reports [100, 101].

Table 1 Overview of recently developed metal oxide photocatalysts for H_2 generation under visible-light illumination

Photocatalsyt	Co-catalyst	Sacrificial reagent	H_2 evolution/ μmol h^{-1}	Ref.
$K_4Nb_6O_{17}$	tris(2,2′-bipyridyl)ruthenium(II) chloride	EDTA	3.6	[127]
$SrTiO_3$:Cr/Ta	Pt	CH_3OH	140	[128]
$SrTiO_3$:Cr/Sb	Pt	CH_3OH	156	[129]
$SrTiO_3$:Ni/Ta	Pt	CH_3OH	2.4	[130]
$SrTiO_3$:Rh	Pt	CH_3OH	117	[131]
$CaTiO_3$:Rh	Pt	CH_3OH	8.5	[132]
$La_2Ti_2O_7$:Cr	Pt	CH_3OH	30	[133]
$La_2Ti_2O_7$:Fe	Pt	CH_3OH	20	[133]
$Sm_2Ti_2S_2O_5$	Pt	CH_3OH	40	[134]
$PbTiO_3$	Pt	CH_3OH	13.6	[135]
$In_{0.9}Ni_{0.1}TaO_4$	NiO, RuO_2	–	16.6	[136, 137]
$K_{0.5}La_{0.25}Bi_{0.25}Ca_{0.75}Pb_{0.75}Nb_3O_{10}$	Pt	CH_3OH	168	[135]
$PbBi_2Nb_2O_9$	Pt	CH_3OH	7.6	[138]
In_2O_3/Cr:In_2O_3	NiO, Pt	CH_3OH	0.36	[139]
$Ba_2In_2O_5$	NiO, Pt	CH_3OH	3.2	[139]
$RbPb_2Nb_3O_{10}$	Pt	CH_3OH	4	[140]
$SnNb_2O_6$	Pt	CH_3OH	14.4	[141–143]
$AgNbO_3$	Pt	CH_3OH	8.2	[144]
$Sn^{2+}/K_4Nb_6O_{17}$	Pt	CH_3OH	23	[145]
$Sn^{2+}/KTiNbO_5$	Pt	CH_3OH	54	[145]
$Sn^{2+}/CsTi_2NbO_7$	Pt	CH_3OH	18	[145]
$Sn^{2+}/K_2Ti_4O_9$	Pt	CH_3OH	23	[145]
$Sn^{2+}/K_2Ti_4O_9$	Pt	CH_3OH	5	[145]
$Sn^{2+}/Cs_2Ti_6O_{13}$	Pt	CH_3OH	7	[145]

Herein, we summarize the more recent publications related to the oxynitride and oxysulfide photocatalysts.

Takanabe et al. studied the photocatalytic water-splitting reactions over the $(Zn_{1+x}Ge)(N_2O_x)$ photocatalyst [102]. The photocatalyst showed high rates for overall water splitting under visible irradiation. Their results showed negligible changes in the structure and composition of the photocatalyst after the photocatalytic reaction. The photocatalytic activity was improved by metal doping in the oxynitride formulation and post-calcination after nitridation. The improvement of photocatalytic activity was ascribed to the reduction of the number of defects in the photocatalyst materials.

TaON nanotube arrays (shown in Fig. 26) were synthesized via sono-electrochemical anodization followed by nitridation [103]. They exhibited efficient performance for photoelectrochemical generation of hydrogen from water.

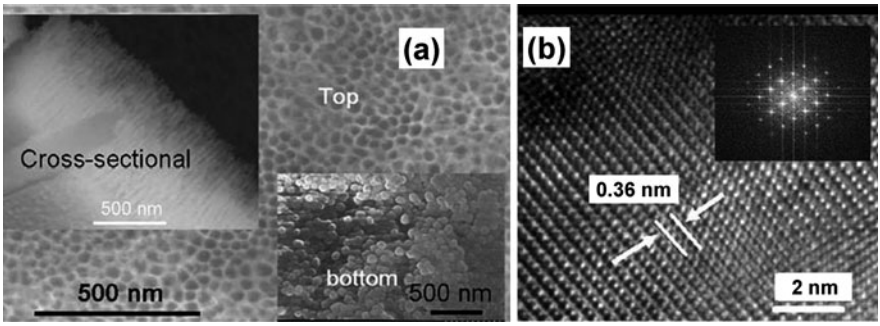

Fig. 26 **a** FESEM images of TaON nanotube arrays on Ta foil. The *insets* show the cross sectional image of Ta_2O_5 NT arrays. **b** HRTEM and FFT pattern of TaON NTs. Ref. [103]—reproduced by permission of The Royal Society of Chemistry

The photocatalytic activity of $(Ga_{1-x}Zn_x)(N_{1-x}O_x)$, a solid solution of GaN and ZnO, for H_2 evolution in the presence of methanol as a sacrificial reagent under visible light was investigated in detail [104]. $(Ga_{1-x}Zn_x)(N_{1-x}O_x)$ evolved H_2 from an aqueous methanol solution when loaded with nanoparticulate $Rh_{2-y}Cr_yO_3$ as a cocatalyst. The H_2 evolution activity was strongly dependent on the crystallinity and composition of the catalyst. The quantum efficiency for overall water splitting increased to 2.5% at 420–440 nm [105]. This represented a tenfold increase in efficiency over the highest efficiency previously obtained using nanoparticulate RuO_2 as a cocatalyst. Besides, the dispersion and size of cocatalyst nanoparticles were identified as important factors affecting the degree of enhancement for stoichiometric water splitting. The results of photocatalytic reactions and photoelectrochemical measurements suggested that the rate-determining step for overall water splitting using $(Ga_{1-x}Zn_x)(N_{1-x}O_x)$ was the H_2 evolution process [105].

Lee et al. developed a zinc germanium oxynitride, a solid solution between ZnO and $ZnGeN_2$, through a reaction of GeO_2 and ZnO under an NH_3 flow [106]. The samples nitrided for 5–15 h under these conditions exhibited a single phase of wurtzitic $(Zn_{1+x}Ge)(N_2O_x)$ and were responsive to visible light with a band gap of ca. 2.7–2.8 eV. Nitridation for 15 h afforded $(Zn_{1+x}Ge)(N_2O_x)$ with the highest photocatalytic activity for overall water splitting. A variety of cocatalysts were also examined, and $Rh_{2-x}Cr_xO_3$ was identified as the most effective cocatalyst for $(Zn_{1+x}Ge)(N_2O_x)$, which caused an increase in the activity for hydrogen evolution. Modification of the optimized $(Zn_{1.44}Ge)(N_{2.08}O_{0.38})$ sample by loading with $Rh_{2-x}Cr_xO_3$ (3.0 wt% Rh, 0.2 wt% Cr) resulted in an effective photocatalyst for overall water decomposition with a quantum efficiency of ca. 0.20% at 420 nm.

A rose-red color $Nb_2Zr_6O_{17-x}N_x$ oxynitride photocatalyst was synthesized by thermal ammonolysis of $Nb_2Zr_6O_{17}$ at 1073 K [107]. TEM images of the $Nb_2Zr_6O_{17-x}N_x$ sample showed prismatic pseudo orthorhombic shaped particles with clear edges and an average particle size in the range of 80–90 nm. The oxynitride $Nb_2Zr_6O_{17-x}N_x$ gave a quantum yield of 13.5% in the production of

Table 2 Sulfide photocatalysts for H_2 evolution from aqueous solutions in the presence of sacrificial reagents

Photocatalyst	BG/eV	Incident light/nm	Light source	Reactant solution	H_2 evolution/μmol h^{-1}	QY (%)	Ref.
$Mn_{0.9}Cd_{0.1}S$	2.2	>420	500 W Xe	$Na_2S + Na_2SO_3$	71	7	[146]
CuS(5.9%)-$Zn_{0.65}Cd_{0.35}S$:Pt	2.5	>420	300 W Xe	$Na_2S + Na_2SO_3$	740	19	[147]
PdS(0.13%)/CdS:Pt	2.3	>420	300 W Xe	$Na_2S + Na_2SO_3$	8770	93	[148]
$ZnS_{-1x-0.5y}O_x(OH)_y$(1:1)	2.2	>420	400 W metal halide lamp	$Na_2S + Na_2SO_3$	14	3	[149]
$Cd_{0.7}Zn_{0.3}S$	2.6		300 W arc lamp	$Na_2S + Na_2SO_3$	350	–	[150]
$Cd_{0.1}Zn_{0.9}S:Ni^{2+}$	2.4	>420	350 W Xe	$Na_2S + Na_2SO_3$	585	16	[151]
$AgGa_{0.9}In_{0.1}S_2$:Pt	2.4	>420	450 W Hg	$Na_2S + Na_2SO_3$	350	–	[152]
$Cd_{0.8}Zn_{0.2}S$	2.5	>430	350 W Xe	$Na_2S + Na_2SO_3$	190	10	[153]
ZnS:Cu	–	>400	550 W Xe	$Na_2S + Na_2SO_3$	650	–	[154]
CdS:Pt	2.3	>420	300 W Xe	$Na_2S + Na_2SO_3$	4100	60	[155]
$AgIn_5S_8$:Pt	1.8	>420	400 W Xe	$Na_2S + K_2SO_3$	60	5.3	[156]
$ZnS:Ni^{2+}$		>400	300 W Xe	$Na_2S + K_2SO_3$	18	2.1	[157]

hydrogen from the decomposition of hydrogen sulfide under visible-light irradiation. A d^0–d^{10} complex photocatalyst, zinc, and titanium spinel oxynitride ($Zn_xTiO_yN_z$) reduced H^+ to H_2 in the presence of a sacrificial electron donor under visible-light irradiation [108]. Ogisu et al. reported a lanthanum–indium oxysulfide visible-light-driven ($420 < \lambda < 480$ nm) photocatalyst for water splitting. Loading with Pt is effective for promoting H_2 evolution [99].

3.1.3 Metal Sulfide Photocatalysts

Metal sulfides photocatalysts have been widely studied due to their outstanding performance in hydrogen generation via photocatalysis. The VB usually consists of S 3p orbitals the level of which is more negative than O 2p. The photocorrosion problem is usually solved by adding sacrificial reagents such as S^{2-} and SO_3^{2-} into the water-splitting system. Many visible-light-driven metal sulfide photocatalysts have been summarized in a previous report [2]. Table 2 lists the new photocatalysts reported in the last 3 years.

3.1.4 Polymeric Photocatalysts

Synthetic polymer semiconductors such as polyparaphenylene have also been used for hydrogen production under UV illumination [109]. Recently, a metal-free polymeric, visible-light-driven photocatalyst for hydrogen production was

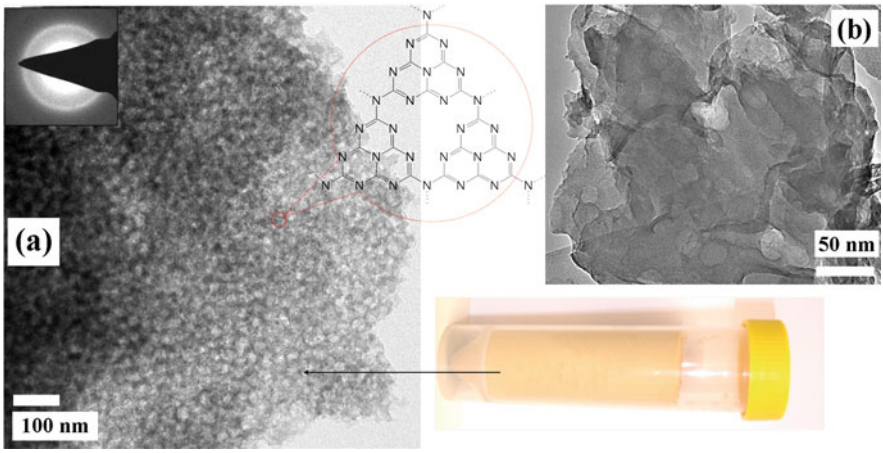

Fig. 27 **a** TEM image of mpg-C_3N_4, showing a 3D porous framework constructed from tri(s)triazine units. The stacking distance of 0.332 nm is evident by the intense electron diffraction ring(*inset*), providing high partial crystallinity of the wall. **b** TEM image of bulk g-C_3N_4. Reprinted with permission from Ref. [110]. Copyright 2009 American Chemical Society

reported [74]. It was a graphitic carbon nitride (g-C_3N_4) synthesized via a thermal polycondensation of cyanamide. The bandgap of g-C_3N_4 was estimated to be 2.7 eV from its ultraviolet–visible spectrum, showing an intrinsic semiconductor-like absorption in the blue region. Different thermal condensation enabled the finer adjustment of the electronic and optical properties. The photocatalyst produced H_2 from water containing triethanolamine as a sacrificial electron donor upon light illumination ($\lambda > 420$ nm) in the absence of noble metal catalysts such as Pt. No N_2 evolution was observed for this catalyst, even after a very long irradiation time, indicating excellent stability due to the strong binding of N in the covalent carbon nitride. This is the first polymeric photocatalyst that is cheap and commonly available. It will open new avenues for organic semiconductors as energy transducers.

However, the quantum yield of the above system (0.1% at 420–460 nm) must be improved. The efficiency of hydrogen production over g-C_3N_4 can be improved by tailoring its nanostructure. A mesoporous structure can enhance the light harvesting ability and mass transfer due to its large surface and multiple scattering effects. Wang et al. advanced g-C_3N_4 by generating a nanoporous structure into the polymeric matrix to improve its structural and electronic functions for solar energy conversion [110]. The photocatalyst mpg-C_3N_4 has a 3D porous framework (shown in Fig. 27), exhibiting an improved efficiency by an order of magnitude. The improved catalytic efficiency was due to the large surface area, which was a basic requirement for a heterogeneous (photo)catalyst to be chemically productive. This example shows excellent artificial photosynthesis over mesoporous polymer semiconductors.

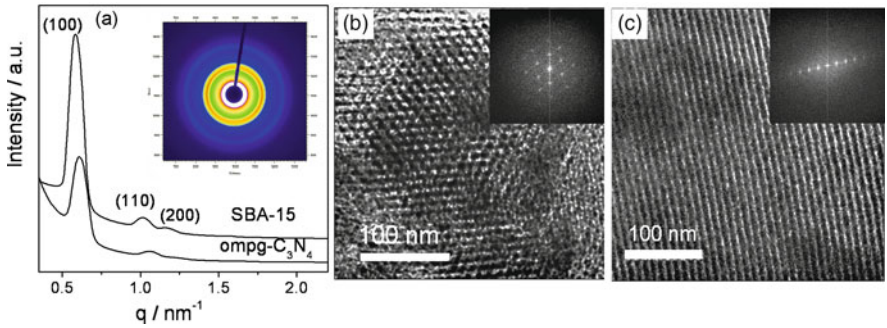

Fig. 28 **a** SAXS patterns of ompg-C_3N_4 and SBA-15 template. The *inset* shows the corresponding 2D SAXS image of ompg-C_3N_4. **b**, **c** Typical TEM images of ompg-C_3N_4. The *insets* show the corresponding fast Fourier transforms of the patterns. Reprinted with permission from Ref. [113]. Copyright 2009 American Chemical Society

The ordered mesostructure permits the structural orientation of guest molecules in the periodic nanopores, which enhances the selectivity and activity in photocatalysis [69, 111, 112]. Very recently, highly ordered porous g-C_3N_4 materials (shown as ompg-C_3N_4 in Fig. 28) were synthesized via a SBA-15 template route [113]. The photocatalytic activity was evaluated by photochemical reduction of water in the presence of an electron donor with visible light [113]. The total evolution of H_2 reached 2.1 mmol during the course of 25 h visible-light irradiation. The H_2 evolution on the ordered mesoporous C_3N_4 was about five times higher than that of bulk g-C_3N_4 [110]. Such a structure is promising as a host semiconductor scaffold for the design of hybrid visible-light photocatalyst. Furthermore, the photocatalyst surface can be functionalized easily via surface reaction or deposition. Various cocatalysts such as chromophoric antenna molecules can be coassembled into the ordered mesoporus carbon nitride, generating new biomimetic photocatalyst systems.

3.2 Solar-Light-Driven Photocatalysts for Valuable Hydrocarbon Evolution from CO_2

In recent years, carbon dioxide emissions from the burning of fossil fuels have grown to $\sim 2.5 \times 10^{10}$ metric tons per annum. This presents a significant environmental challenge for the twenty-first century. In nature, CO_2 is removed from the environment by photosynthesis. The energy obtained from sunlight is ultimately used to convert CO_2 into glucose, a sugar molecule that stores solar energy in the form of chemical energy. However, the efficiency of energy transformation is low. Even under the optimal artificial conditions (microalgae in full sunlight), the energy efficiency is only about 7% [8].

Carbon sequestration is considered a promising interim solution to global warming. It involves the capture and storage of fossil fuel-derived CO_2 emissions to prevent their release into the atmosphere. The captured CO_2 is stored in the oceans or in depleted gas and oil fields. The main drawback of the technology is the temporary nature of the storage. CO_2 stored in the ocean, for example, will inevitably return to the atmosphere in periods estimated from hundreds to thousands of years. Another drawback of ocean storage is the acidic characteristic of dissolved CO_2 and the effects of pH change in seawater on the local environment. Storage of large amounts of non-converted, concentrated CO_2 in oil and gas reservoirs needs continuous monitoring for an infinite time. A sudden release of CO_2 could be lethal, as demonstrated in the 1986 Lake Nyos disaster in Cameroon [114]. Carbon capture and storage will therefore not be commercially available until the cost and safety issues are satisfactorily addressed.

The conversion of CO_2 to useful fuels by physiochemical means not only reduces CO_2 in the atmosphere, but also eases our dependence on oil. The conventional approach involves the thermal hydrogenation of CO_2 into hydrocarbons under relatively high temperatures and pressures [115]. The major problem with the catalytic reduction of CO_2 is that huge amounts of H_2 are required as the reducing agent and in addition fossil fuels are consumed to provide the heat needed for the reaction to proceed.

An attractive alternative to thermal hydrogenation is photocatalytic reduction, especially if this utilizes sunlight. In this approach, CO_2 from industrial waste gases is converted to valuable fuels, such as methane and methanol. These products can be easily transported, stored and used in industry or, in the case of methanol, as a gasoline-additive for automobiles. Moreover, they can be transformed into other useful chemicals by using conventional technologies. This is a perfect solution to both the global warming and energy shortage problems. This section reviews the use of photocatalysts to produce valuable fuels from the virtually free resources of carbon dioxide, water and sunlight. The potential products are methane, methanol, or even longer chain hydrocarbons via a Fisher-Tropsch type condensation. From the viewpoints of both energy and environment, the conversion of CO_2 to fuels by solar energy is an ideal solution to the current global warming and energy crises.

For solar-driven catalytic conversion of CO_2 to fuels to be practical, highly efficient photocatalysts are required. Titania (TiO_2) has been considered the most appropriate candidate due to its powerful oxidizing nature, superior charge transport properties, and corrosion resistance. Earlier studies, however, could only achieve low CO_2 conversion rates in spite of using UV illumination for band gap excitation. Anpo et al. carried out a series of studies on Ti-zeolites and Ti-mesoporous materials [116, 117]. Powdered TiO_2 was also used by Adachi and co-workers as a photocatalyst for the reduction of CO_2 with H_2O. A total hydrocarbon (methane, ethene and ethane) generation rate of about 1.7 μL/(h g) was achieved under xenon lamp illumination when copper-loaded titania nanoparticles were dispersed in CO_2-pressurized water [118]. Tan et al., using titania pellets, obtained a maximum rate of about 0.25 μmol/h of methane from the irradiation of

moist carbon dioxide by monochromatic ultraviolet light (253.7 nm wavelength) [119, 120]. Using UV irradiation of a hydrogen (90%), water, carbon dioxide combination, a rate of 4.1 μmol/(h g) was obtained by Lo and co-workers [121].

Recently, numerous studies on the preparation of solar-light-driven photocatalysts for hydrocarbon formation were reported. They can be classified into two categories: TiO_2-based photocatalysts and composite photocatalysts.

3.2.1 TiO_2-Based Photocatalysts

Metal doped TiO_2 catalyst sensitized with N3 dye was employed to photoreduce CO_2 with H_2O under concentrated natural sunlight to fuels in an optical-fiber photoreactor [122]. A methane production rate of 0.617 μmol/(g h) was achieved on N3-dye-Cu(0.5 wt%)-e(0.5 wt%)/TiO_2 coated onto optical fibers under an average solar light intensity of 20 mW/cm^2. The N3 dye substantially improved the photoactivity of Cu(0.5 wt%)-Fe(0.5 wt%)/TiO_2 catalyst toward methane production under concentrated natural sunlight due to its full visible-light adsorption. The photocatalyst was stable up to 6 h.

Recently, N-doped TiO_2 nanotubes with copper and platinum nanoparticles loaded onto the surfaces were developed to realize efficient solar conversion of carbon dioxide and water vapor to methane and other hydrocarbons [123]. The experiments were conducted in outdoor sunlight at University Park, PA (shown in Fig. 29). Using outdoor global AM 1.5 sunlight, 100 mW/cm^2, a hydrocarbon production rate of 111 ppm cm^{-2} h^{-1}, or ~160 μL/(g h), was obtained when the nanotube array samples were loaded with both 52% Cu and 48% Pt nanoparticles. The authors pointed out that the efficiency of the catalyst was still quite low, but were optimistic that further work could improve it.

3.2.2 Composite Photocatalysts

Carbon dioxide can be reduced with water to organic compounds over a hybrid catalyst under concentrated sunlight [124]. The catalyst was Pt-loaded $K_2Ti_6O_{13}$ coupled with an Fe-based catalyst supported on a dealuminated Y-type zeolite (Fe-Cu-K/DAY) [124]. The Pt/$K_2Ti_6O_{13}$ catalyst decomposed water to produce H_2 and the Fe-Cu-K/DAY catalyst reduced CO_2, with resulting organic compounds of CH_4, HCOOH, HCHO, CH_3OH, and C_2H_5OH. The Pt/$K_2Ti_6O_{13}$ catalysts can be combined with another CO_2 hydrogenation catalyst of Cu/ZnO [125]. The generation of CH_3OH over this composite photocatalyst under concentrated sunlight means successful photocatalytic conversion carbon dioxide to fuels. These studies suggest that sunlight-driven photocatalytic processes have potential for organic compound evolution from CO_2 and water.

Recently, a NiO/$InTaO_4$ photocatalyst with a band gap of 2.6 eV was developed by Chen's Group [126]. The NiO cocatalyst was loaded by incipient-wetness impregnation with an aqueous solution of $Ni(NO_3)_2$. The product was calcined at

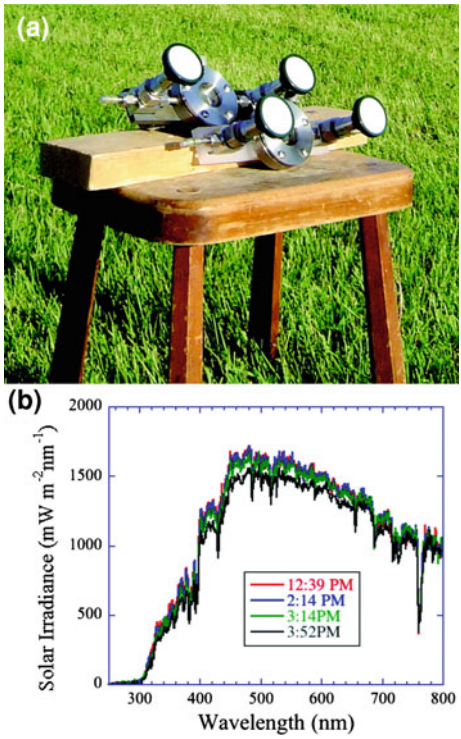

Fig. 29 **a** Digital photograph of the reaction chambers kept under natural sunlight for photocatalytic CO_2 conversion. **b** Spectral irradiance recorded from 12:39 p.m. to 3:52 p.m. for an experiment conducted on September 1, 2008 at University Park, PA. Reprinted with permission from Ref. [123]. Copyright 2009 American Chemical Society

350°C for 1 h in air, and then pretreated by H_2 reduction at 500°C for 2 h and subsequent O_2 oxidation at 200°C for 1 h. This catalyst was able to reduce CO_2 to methanol under visible-light illumination. A 1.0 wt% NiO-$InTaO_4$ photocatalyst in 0.2 M $KHCO_3$ gave the highest activity (1.394 μmol/(h g)) (shown in Fig. 30). The reduction–oxidation pretreatment had a positive effect on the activity of the catalyst.

In summary, the ultimate goal is to design advanced catalysts with high photon efficiencies. For the most promising catalysts the rate limiting steps in the conversions of water and CO_2 need to be determined. Relationships between the photocatalytic efficiency and the characteristics of the catalyst such as morphology, pore structure, surface area, surface electronic states and band gap must be investigated.

4 Summary and Future Prospects

Various photocatalytic semiconductor nanomaterials with great potential for energy and environmental applications have been prepared. Despite the tremendous research efforts on the synthesis and modification of photocatalysts, many

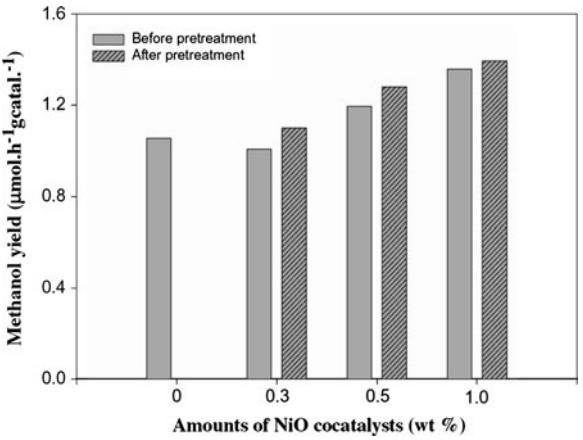

Fig. 30 Methanol yield on NiO-$InTaO_4$ in 0.2 M $KHCO_3$ aqueous solution under visible-light irradiation. Reprinted from Pan and Chen [126], copyright 2007 with permission from Elsevier

problems still exist. This is particularly true with regard to low photocatalytic efficiencies and the lack of understanding of the intrinsic mechanisms for the systems. Thus, the design of novel photocatalytic materials with higher efficiency is a perennial subject of interest in the field of photocatalysis. As more and more attention is paid to energy issues, the development of practical systems for H_2 evolution from water and the photo-reduction of carbon dioxide to fuels cannot be overemphasized. Advanced photocatalytic nanomaterials may be the key to a sustainable future.

Acknowledgments We would like to thank supports from the Research Grants Council of Hong Kong (General Research Fund CUHK404810), the Program for Professor of Special Appointment (Eastern Scholar) at Shanghai Institutions of Higher Learning, and the National Natural Science Foundation of China (21007040).

References

1. Ravelli D, Dondi D, Fagnoni M et al (2009) Photocatalysis. A multi-faceted concept for green chemistry. Chem Soc Rev 38:1999–2011
2. Kudo A, Miseki Y (2009) Heterogeneous photocatalyst materials for water splitting. Chem Soc Rev 38:253–278
3. Han F, Kambala VSR, Srinivasan M et al (2009) Tailored titanium dioxide photocatalysts for the degradation of organic dyes in wastewater treatment: a review. Appl Catal A Gen 359:25–40
4. Hoffmann MR, Martin ST, Choi WY et al (1995) Environmental applications of semiconductor photocatalysis. Chem Rev 95:69–96
5. Yu HT, Quan X (2009) Nano-heterojunction photocatalytic materials in environmental pollution controlling. Prog Chem 21:406–419
6. Fujishima A, Zhang XT, Tryk DA (2008) TiO_2 photocatalysis and related surface phenomena. Surf Sci Rep 63:515–582
7. Hernandez-Alonso MD, Fresno F, Suarez S et al (2009) Development of alternative photocatalysts to TiO_2: challenges and opportunities. Energy Environ Sci 2:1231–1257

8. Wu JCS (2009) Photocatalytic reduction of greenhouse gas CO_2 to fuel. Catal Surv Asia 13:30–40
9. Osterloh FE (2008) Inorganic materials as catalysts for photochemical splitting of water. Chem Mater 20:35–54
10. Chen X, Mao SS (2007) Titanium dioxide nanomaterials: synthesis, properties, modifications, and applications. Chem Rev 107:2891–2959
11. Yu JG, Xiang QJ, Zhou MH (2009) Preparation, characterization and visible-light-driven photocatalytic activity of Fe-doped titania nanorods and first-principles study for electronic structures. Appl Catal B Environ 90:595–602
12. Yang Y, Wang HY, Li X et al (2009) Electrospun mesoporous w^{6+}-doped TiO_2 thin films for efficient visible-light photocatalysis. Mater Lett 63:331–333
13. Tian BZ, Li CZ, Gu F et al (2009) Flame sprayed V-doped TiO_2 nanoparticles with enhanced photocatalytic activity under visible light irradiation. Chem Eng J 151:220–227
14. Tian BZ, Li CZ, Gu F et al (2009) Visible-light photocatalytic activity of Cr-doped TiO_2 nanoparticles synthesized by flame spray pyrolysis. J Inorg Mater 24:661–665
15. Lorret O, Francova D, Waldner G et al (2009) W-doped titania nanoparticles for UV and visible-light photocatalytic reactions. Appl Catal B Environ 91:39–46
16. Li JX, Xu JH, Dai WL et al (2009) Direct hydro-alcohol thermal synthesis of special core-shell structured Fe-doped titania microspheres with extended visible light response and enhanced photoactivity. Appl Catal B Environ 85:162–170
17. Khan MA, Han DH, Yang OB (2009) Enhanced photoresponse towards visible light in Ru doped titania nanotube. Appl Surf Sci 255:3687–3690
18. Xu JJ, Ao YH, Chen MD (2009) Preparation of B-doped titania hollow sphere and its photocatalytic activity under visible light. Mater Lett 63:2442–2444
19. Park Y, Kim W, Park H et al (2009) Carbon-doped TiO_2 photocatalyst synthesized without using an external carbon precursor and the visible light activity. Appl Catal B Environ 91:355–361
20. Tafen DN, Wang J, Wu NQ et al (2009) Visible light photocatalytic activity in nitrogen-doped TiO_2 nanobelts. Appl Phys Lett 94:093101.1–093101.3
21. Lv YY, Yu LS, Huang HY et al (2009) Preparation of F-doped titania nanoparticles with a highly thermally stable anatase phase by alcoholysis of $TiCl_4$. Appl Surf Sci 255:9548–9552
22. Li HX, Zhang XY, Huo YN et al (2007) Supercritical preparation of a highly active S-doped TiO_2 photocatalyst for methylene blue mineralization. Environ Sci Technol 41:4410–4414
23. Tian GH, Pan K, Fu HG et al (2009) Enhanced photocatalytic activity of S-doped TiO_2-ZrO_2 nanoparticles under visible-light irradiation. J Hazard Mater 166:939–944
24. Xu JJ, Ao YH, Fu DG et al (2008) Low-temperature preparation of F-doped TiO_2 film and its photocatalytic activity under solar light. Appl Surf Sci 254:3033–3038
25. Wu GS, Chen A (2008) Direct growth of F-doped TiO_2 particulate thin films with high photocatalytic activity for environmental applications. J Photoch Photobio A Chem 195:47–53
26. Cui Y, Du H, Wen LS (2009) Origin of visible-light-induced photocatalytic properties of S-doped anatase TiO_2 by first-principles investigation. Solid State Commun 149:634–637
27. Liu G, Yang HG, Wang XW et al (2009) Visible light responsive nitrogen doped anatase TiO_2 sheets with dominant 001 facets derived from tin. J Am Chem Soc 131:12868–12869
28. Ho W, Yu JC, Lee S (2006) Synthesis of hierarchical nanoporous F-doped TiO_2 spheres with visible light photocatalytic activity. Chem Commun 1115–1117
29. Ho WK, Yu JC, Lee SC (2006) Low-temperature hydrothermal synthesis of S-doped TiO_2 with visible light photocatalytic activity. J Solid State Chem 179:1171–1176
30. Asahi R, Morikawa T, Ohwaki T et al (2001) Visible-light photocatalysis in nitrogen-doped titanium oxides. Science 293:269–271
31. Yamashita H, Harada M, Misaka J et al (2002) Degradation of propanol diluted in water under visible light irradiation using metal ion-implanted titanium dioxide photocatalysts. J Photochem Photobiol A Chem 148:257–261

32. Sakthivel S, Kisch H (2003) Daylight photocatalysis by carbon-modified titanium dioxide. Angew Chem Int Ed 42:4908–4911
33. Yamashita H, Harada M, Misaka J et al (2003) Photocatalytic degradation of organic compounds diluted in water using visible light-responsive metal ion-implanted TiO_2 catalysts: Fe ion-implanted TiO_2. Catal Today 84:191–196
34. Hong XT, Wang ZP, Cai WM et al (2005) Visible-light-activated nanoparticle photocatalyst of iodine-doped titanium dioxide. Chem Mater 17:1548–1552
35. Chai SY, Kim YJ, Jung MH et al (2009) Heterojunctioned $BiOCl/Bi_2O_3$, a new visible light photocatalyst. J Catal 262:144–149
36. Lin XP, Xing JC, Wang WD et al (2007) Photocatalytic activities of heterojunction semiconductors $Bi_2O_3/BaTiO_3$: a strategy for the design of efficient combined photocatalysts. J Phys Chem C 111:18288–18293
37. Pal B, Hata T, Goto K et al (2001) Photocatalytic degradation of o-cresol sensitized by iron-titania binary photocatalysts. J Mol Catal A Chem 169:147–155
38. Bessekhouad Y, Robert D, Weber J (2004) Bi_2S_3/TiO_2 and CdS/TiO_2 heterojunctions as an available configuration for photocatalytic degradation of organic pollutant. J Photochem Photobiol A Chem 163:569–580
39. Zhang HT, Ouyanga SX, Lia ZS et al (2006) Preparation, characterization and photocatalytic activity of polycrystalline $Bi_2O_3/SrTiO_3$ composite powders. J Phys Chem Solids 67:2501–2505
40. Zhang ML, An TC, Hu XH et al (2004) Preparation and photocatalytic properties of a nanometer ZnO-SnO_2 coupled oxide. Appl Catal A Gen 260:215–222
41. Li GS, Zhang DQ, Yu JC (2009) A new visible-light photocatalyst: CdS quantum dots embedded mesoporous TiO_2. Environ Sci Technol 43:7079–7085
42. Zong X, Yan HJ, Wu GP et al (2008) Enhancement of photocatalytic H_2 evolution on CdS by loading MoS_2 as cocatalyst under visible light irradiation. J Am Chem Soc 130:7176–7177
43. Huang HJ, Li DZ, Lin Q et al (2009) Efficient degradation of benzene over $LaVO_4/TiO_2$ nanocrystalline heterojunction photocatalyst under visible light irradiation. Environ Sci Technol 43:4164–4168
44. Huang HJ, Li DZ, Lin Q et al (2009) Efficient photocatalytic activity of PZT/TiO_2 heterojunction under visible light irradiation. J Phys Chem C 113:14264–14269
45. Kim YJ, Gao B, Han SY et al (2009) Heterojunction of $FeTiO_3$ nanodisc and TiO_2 nanoparticle for a novel visible light photocatalyst. J Phys Chem C 113:19179–19184
46. Rawal SB, Chakraborty AK, Lee WI (2009) Heterojunction of FeOOH and TiO_2 for the formation of visible light photocatalyst. Bull Korean Chem Soc 30:2613–2616
47. Tsunoda Y, Sugimoto W, Sugahara Y (2003) Intercalation behavior of n-alkylamines into a protonated form of a layered perovskite derived from aurivillius phase $Bi_2SrTa_2O_9$. Chem Mater 15:632–635
48. Kim JY, Chung I, Choy JH et al (2001) Macromolecular nanoplatelet of Aurivillius-type layered perovskite oxide, $Bi_4Ti_3O_{12}$. Chem Mater 13:2759–2761
49. Zhang C, Zhu YF (2005) Synthesis of square Bi_2WO_6 nanoplates as high-activity visible-light-driven photocatalysts. Chem Mater 17:3537–3545
50. Yu JG, Xiong JF, Cheng B et al (2005) Hydrothermal preparation and visible-light photocatalytic activity of Bi_2WO_6 powders. J Solid State Chem 178:1968–1972
51. Fu HB, Pan CS, Yao WQ et al (2005) Visible-light-induced degradation of rhodamine B by nanosized Bi_2WO_6. J Phys Chem B 109:22432–22439
52. Kudo A, Hijii S (1999) H_2 or O_2 evolution from aqueous solutions on layered oxide photocatalysts consisting of Bi^{3+} with $6s^2$ configuration and d^0 transition metal ions. Chem Lett 1103–1104
53. Tang JW, Zou ZG, Ye JH (2004) Photocatalytic decomposition of organic contaminants by Bi_2WO_6 under visible light irradiation. Catal Lett 92:53–56
54. Zhang LH, Wang WZ, Chen ZG et al (2007) Fabrication of flower-like Bi_2WO_6 superstructures as high performance visible-light driven photocatalysts. J Mater Chem 17:2526–2532

55. Wu J, Duan F, Zheng Y et al (2007) Synthesis of Bi_2WO_6 nanoplate-built hierarchical nest-like structures with visible-light-induced photocatalytic activity. J Phys Chem C 111:12866–12871
56. Zhang LS, Wang WZ, Zhou L et al (2007) Bi_2WO_6 nano- and microstructures: shape control and associated visible-light-driven photocatalytic activities. Small 3:1618–1625
57. Zhu SB, Xu TG, Fu HB et al (2007) Synergetic effect of Bi_2WO_6 photocatalyst with C_{60} and enhanced photoactivity under visible irradiation. Environ Sci Technol 41:6234–6239
58. Hasobe T, Imahori H, Fukuzumi S et al (2003) Light energy conversion using mixed molecular nanoclusters. Porphyrin and C_{60} cluster films for efficient photocurrent generation. J Phys Chem B 107:12105–12112
59. Shi R, Huang GL, Lin J et al (2009) Photocatalytic activity enhancement for Bi_2WO_6 by fluorine substitution. J Phys Chem C 113:19633–19638
60. Li JP, Zhang X, Ai ZH et al (2007) Efficient visible light degradation of rhodamine B by a photo-electrochemical process based on a Bi_2WO_6 nanoplate film electrode. J Phys Chem C 111:6832–6836
61. Shang M, Wang WZ, Ren J et al (2009) A practical visible-light-driven Bi_2WO_6 nanofibrous mat prepared by electrospinning. J Mater Chem 19:6213–6218
62. Kudo A, Omori K, Kato H (1999) A novel aqueous process for preparation of crystal form-controlled and highly crystalline $BiVO_4$ powder from layered vanadates at room temperature and its photocatalytic and photophysical properties. J Am Chem Soc 121:11459–11467
63. Kohtani S, Koshiko M, Kudo A et al (2003) Photodegradation of 4-alkylphenols using $BiVO_4$ photocatalyst under irradiation with visible light from a solar simulator. Appl Catal B Environ 46:573–586
64. Tokunaga S, Kato H, Kudo A (2001) Selective preparation of monoclinic and tetragonal $BiVO_4$ with scheelite structure and their photocatalytic properties. Chem Mater 13:4624–4628
65. Lim AR, Choh SH, Jang MS (1995) Prominent ferroelastic domain-walls in $BiVO_4$ crystal. J Phys Condens Mat 7:7309–7323
66. Liu JB, Wang H, Wang S et al (2003) Hydrothermal preparation of $BiVO_4$ powders. Mater Sci Eng B 104:36–39
67. Sayama K, Nomura A, Zou ZG et al (2003) Photoelectrochemical decomposition of water on nanocrystalline $BiVO_4$ film electrodes under visible light. Chem Commun 2908–2909
68. Zhou L, Wang WZ, Zhang L et al (2007) Single-crystalline $BiVO_4$ microtubes with square cross-sections: microstructure, growth mechanism, and photocatalytic property. J Phys Chem C 111:13659–13664
69. Li GS, Zhang DQ, Yu JC (2008) Ordered mesoporous $BiVO_4$ through nanocasting: a superior visible light-driven photocatalyst. Chem Mater 20:3983–3992
70. Zhou L, Wang WZ, Xu HL (2008) Controllable synthesis of three-dimensional well-defined $BiVO_4$ mesocrystals via a facile additive-free aqueous strategy. Cryst Growth Des 8:728–733
71. Dunkle SS, Helmich RJ, Suslick KS (2009) $BiVO_4$ as a visible-light photocatalyst prepared by ultrasonic spray pyrolysis. J Phys Chem C 113:11980–11983
72. Xu H, Li HM, Wu CD et al (2008) Preparation, characterization and photocatalytic properties of Cu-loaded $BiVO_4$. J Hazard Mater 153:877–884
73. Ge L (2008) Novel visible-light-driven Pt/$BiVO_4$ photocatalyst for efficient degradation of methyl orange. J Mol Catal A Chem 282:62–66
74. Wang XC, Maeda K, Thomas A et al (2009) A metal-free polymeric photocatalyst for hydrogen production from water under visible light. Nat Mater 8:76–80
75. Goettmann F, Fischer A, Antonietti M et al (2006) Chemical synthesis of mesoporous carbon nitrides using hard templates and their use as a metal-free catalyst for Friedel-Crafts reaction of benzene. Angew Chem Int Ed 45:4467–4471
76. Groenewolt M, Antonietti M (2005) Synthesis of g-C_3N_4 nanoparticles in mesoporous silica host matrices. Adv Mater 17:1789–1792

77. Wang XC, Chen XF, Thomas A et al (2009) Metal-containing carbon nitride compounds: a new functional organic-metal hybrid material. Adv Mater 21:1609–1612
78. Yamamoto S, Andersson K, Bluhm H et al (2007) Hydroxyl-induced wetting of metals by water at near-ambient conditions. J Phys Chem C 111:7848–7850
79. Chen XF, Zhang JS, Fu XZ et al (2009) Fe-g-C_3N_4-catalyzed oxidation of benzene to phenol using hydrogen peroxide and visible light. J Am Chem Soc 131:11658–11659
80. Goettmann F, Thomas A, Antonietti M (2007) Metal-free activation CO_2 by mesoporous graphitic carbon nitride. Angew Chem Int Ed 46:2717–2720
81. Liu ZF, Zhao ZG, Miyauchi M (2009) Efficient visible light active $CaFe_2O_4/WO_3$ based composite photocatalysts: effect of interfacial modification. J Phys Chem C 113:17132–17137
82. Zheng LR, Zheng YH, Chen CQ et al (2009) Network structured SnO_2/ZnO heterojunction nanocatalyst with high photocatalytic activity. Inorg Chem 48:1819–1825
83. Zheng YH, Chen CQ, Zhan YY et al (2008) Photocatalytic activity of Ag/ZnO heterostructure nanocatalyst: correlation between structure and property. J Phys Chem C 112:10773–10777
84. Eisenberg R (2009) Rethinking water splitting. Science 324:44–45
85. Maeda K, Teramura K, Lu DL et al (2006) Photocatalyst releasing hydrogen from water—enhancing catalytic performance holds promise for hydrogen production by water splitting in sunlight. Nature 440:295
86. Kudo A, Kato H, Tsuji I (2004) Strategies for the development of visible-light-driven photocatalysts for water splitting. Chem Lett 33:1534–1539
87. Hitoki G, Takata T, Kondo JN et al (2002) (Oxy)nitrides as new photocatalysts for water splitting under visible light irradiation. Electrochemistry 70:463–465
88. Yamasita D, Takata T, Hara M et al (2004) Recent progress of visible-light-driven heterogeneous photocatalysts for overall water splitting. Solid State Ionics 172:591–595
89. Yerga RMN, Galvan MCA, del Valle F et al (2009) Water splitting on semiconductor catalysts under visible-light irradiation. ChemSusChem 2:471–485
90. Kasahara A, Nukumizu K, Hitoki G et al (2002) Photoreactions on $LaTiO_2N$ under visible light irradiation. J Phys Chem A 106:6750–6753
91. Hitoki G, Takata T, Kondo JN et al (2002) An oxynitride, TaON, as an efficient water oxidation photocatalyst under visible light irradiation (lambda $\leq$ 500 nm). Chem Commun 1698–1699
92. Hara M, Nunoshige J, Takata T et al (2003) Unusual enhancement of H_2 evolution by Ru on TaON photocatalyst under visible light irradiation. Chem Commun 3000–3001
93. Hara M, Takata T, Kondo JN et al (2004) Photocatalytic reduction of water by TaON under visible light irradiation. Catal Today 90:313–317
94. Takata T, Hitoki G, Kondo JN et al (2007) Visible-light-driven photocatalytic behavior of tantalum-oxynitride and nitride. Res Chem Intermed 33:13–25
95. Liu MY, You WS, Lei ZB et al (2004) Water reduction and oxidation on Pt-Ru/$Y_2Ta_2O_5N_2$ catalyst under visible light irradiation. Chem Commun 2192–2193
96. Nukumizu K, Nunoshige J, Takata T et al (2003) $TiN_xO_yF_z$ as a stable photocatalyst for water oxidation in visible light (<570 nm). Chem Lett 32:196–197
97. Maeda K, Shimodaira Y, Lee B et al (2007) Studies on $TiN_xO_yF_z$ as a visible-light-responsive photocatalyst. J Phys Chem C 111:18264–18270
98. Ishikawa A, Yamada Y, Takata T et al (2003) Novel synthesis and photocatalytic activity of oxysulfide $Sm_2Ti_2S_2O_5$. Chem Mater 15:4442–4446
99. Ogisu K, Ishikawa A, Teramura K et al (2007) Lanthanum–indium oxysulfide as a visible light driven photocatalyst for water splitting. Chem Lett 36:854–855
100. Maeda K, Teramura K, Saito N et al (2006) Overall water splitting using (oxy)nitride photocatalysts. Pure Appl Chem 78:2267–2276
101. Maeda K, Domen K (2007) New non-oxide photocatalysts designed for overall water splitting under visible light. J Phys Chem C 111:7851–7861

102. Takanabe K, Uzawa T, Wang XC et al (2009) Enhancement of photocatalytic activity of zinc-germanium oxynitride solid solution for overall water splitting under visible irradiation. Dalton Trans 10055–10062
103. Banerjee S, Mohapatra SK, Misra M (2009) Synthesis of TaON nanotube arrays by sonoelectrochemical anodization followed by nitridation: a novel catalyst for photoelectrochemical hydrogen generation from water. Chem Commun 7137–7139
104. Maeda K, Hashiguchi H, Masuda H et al (2008) Photocatalytic activity of $(Ga_{1-x}Zn_x)(N_{1-x}O_x)$ for visible-light-driven H_2 and O_2 evolution in the presence of sacrificial reagents. J Phys Chem C 112:3447–3452
105. Maeda K, Teramura K, Domen K (2007) Development of cocatalysts for photocatalytic overall water splitting on $(Ga_{1-x}Zn_x)(N_{1-x}O_x)$ solid solution. Catal Surv Asia 11:145–157
106. Lee YG, Teramura K, Hara M et al (2007) Modification of $(Zn_{1+x}Ge)(N_2O_x)$ solid solution as a visible light driven photocatalyst for overall water splitting. Chem Mater 19:2120–2127
107. Kanade KG, Baeg JO, Kale BB et al (2007) Rose-red color oxynitride $Nb_2Zr_6O_{17-x}N_x$: a visible light photocatalyst to hydrogen production. Int J Hydrogen Energ 32:4678–4684
108. Hisatomi T, Hasegawa K, Teramura K et al (2007) Zinc and titanium spinel oxynitride $(Zn_xTiO_yN_z)$ as a d^0–d^{10} complex photocatalyst with visible light activity. Chem Lett 36:558–559
109. Yanagida S, Kabumoto A, Mizumoto K et al (1985) Poly(para-phenylene)-catalyzed photoreduction of water to hydrogen. J Chem Soc Chem Commun 474–475
110. Wang XC, Maeda K, Chen XF et al (2009) Polymer semiconductors for artificial photosynthesis: hydrogen evolution by mesoporous graphitic carbon nitride with visible light. J Am Chem Soc 131:1680–1681
111. Yu JC, Wang XC, Fu XZ (2004) Pore-wall chemistry and photocatalytic activity of mesoporous titania molecular sieve films. Chem Mater 16:1523–1530
112. Jun YS, Hong WH, Antonietti M et al (2009) Mesoporous, 2D hexagonal carbon nitride and titanium nitride/carbon composites. Adv Mater 21:4270–4274
113. Chen XF, Jun YS, Takanabe K et al (2009) Ordered mesoporous SBA-15 type graphitic carbon nitride: a semiconductor host structure for photocatalytic hydrogen evolution with visible light. Chem Mater 21:4093–4095
114. Kling GW, Clark MA, Compton HR et al (1987) The 1986 Lake Nyos gas disaster in Cameroon, West-Africa. Science 236:169–175
115. Freund HJ, Roberts MW (1996) Surface chemistry of carbon dioxide. Surf Sci Rep 25:225–273
116. Anpo M, Yamashita H, Ichihashi Y et al (1997) Photocatalytic reduction of CO_2 with H_2O on titanium oxides anchored within micropores of zeolites: effects of the structure of the active sites and the addition of Pt. J Phys Chem B 101:2632–2636
117. Ikeue K, Yamashita H, Anpo M et al (2001) Photocatalytic reduction of CO_2 with H_2O on Ti-beta zeolite photocatalysts: effect of the hydrophobic and hydrophilic properties. J Phys Chem B 105:8350–8355
118. Adachi K, Ohta K, Mizuno T (1994) Photocatalytic reduction of carbon-dioxide to hydrocarbon using copper-loaded titanium-dioxide. Sol Energy 53:187–190
119. Tan SS, Zou L, Hu E (2007) Photosynthesis of hydrogen and methane as key components for clean energy system. Sci Technol Adv Mater 8:89–92
120. Tan SS, Zou L, Hu E (2006) Photocatalytic reduction of carbon dioxide into gaseous hydrocarbon using TiO_2 pellets. Catal Today 115:269–273
121. Lo CC, Hung CH, Yuan CS et al (2007) Photoreduction of carbon dioxide with H_2 and H_2O over TiO_2 and ZrO_2 in a circulated photocatalytic reactor. Sol Energy Mater Sol Cells 91:1765–1774
122. Nguyen TV, Wu JCS, Chiou CH (2008) Photoreduction of CO_2 over ruthenium dye-sensitized TiO_2-based catalysts under concentrated natural sunlight. Catal Commun 9:2073–2076
123. Varghese OK, Paulose M, LaTempa TJ et al (2009) High-rate solar photocatalytic conversion of CO_2 and water vapor to hydrocarbon fuels. Nano Lett 9:731–737

124. Guan GQ, Kida T, Yoshida A (2003) Reduction of carbon dioxide with water under concentrated sunlight using photocatalyst combined with Fe-based catalyst. Appl Catal B Environ 41:387–396
125. Guan GQ, Kida T, Harada T et al (2003) Photoreduction of carbon dioxide with water over $K_2Ti_6O_{13}$ photocatalyst combined with Cu/ZnO catalyst under concentrated sunlight. Appl Catal A Gen 249:11–18
126. Pan PW, Chen YW (2007) Photocatalytic reduction of carbon dioxide on NiO/$InTaO_4$ under visible light irradiation. Catal Commun 8:1546–1549
127. Maeda K, Eguchi M, Youngblood WJ et al (2008) Niobium oxide nanoscrolls as building blocks for dye-sensitized hydrogen production from water under visible light irradiation. Chem Mater 20:6770–6778
128. Ishii T, Kato H, Kudo A (2004) H_2 evolution from an aqueous methanol solution on $SrTiO_3$ photocatalysts codoped with chromium and tantalum ions under visible light irradiation. J Photochem Photobiol A Chem 163:181–186
129. Kato H, Kudo A (2002) Visible-light-response and photocatalytic activities of TiO_2 and $SrTiO_3$ photocatalysts codoped with antimony and chromium. J Phys Chem B 106:5029–5034
130. Niishiro R, Kato H, Kudo A (2005) Nickel and either tantalum or niobium-codoped TiO_2 and $SrTiO_3$ photocatalysts with visible-light response for H_2 or O_2 evolution from aqueous solutions. Phys Chem Chem Phys 7:2241–2245
131. Konta R, Ishii T, Kato H et al (2004) Photocatalytic activities of noble metal ion doped $SrTiO_3$ under visible light irradiation. J Phys Chem B 108:8992–8995
132. Nishimoto S, Matsuda M, Miyake M (2006) Photocatalytic activities of Rh-doped $CaTiO_3$ under visible light irradiation. Chem Lett 35:308–309
133. Hwang DW, Kirn HG, Lee JS et al (2005) Photocatalytic hydrogen production from water over M-doped $La_2Ti_2O_7$ (M = Cr, Fe) under visible light irradiation (lambda > 420 nm). J Phys Chem B 109:2093–2102
134. Ishikawa A, Takata T, Kondo JN et al (2002) Oxysulfide $Sm_2Ti_2S_2O_5$ as a stable photocatalyst for water oxidation and reduction under visible light irradiation (lambda <= 650 nm). J Am Chem Soc 124:13547–13553
135. Kim HG, Becker OS, Jang JS et al (2006) A generic method of visible light sensitization for perovskite-related layered oxides: substitution effect of lead. J Solid State Chem 179:1214–1218
136. Zou ZG, Arakawa H (2003) Direct water splitting into H_2 and O_2 under visible light irradiation with a new series of mixed oxide semiconductor photocatalysts. J Photochem Photobiol A Chem 158:145–162
137. Zou ZG, Ye JH, Sayama K et al (2001) Direct splitting of water under visible light irradiation with an oxide semiconductor photocatalyst. Nature 414:625–627
138. Kim HG, Hwang DW, Lee JS (2004) An undoped, single-phase oxide photocatalyst working under visible light. J Am Chem Soc 126:8912–8913
139. Wang DF, Zou ZG, Ye JH (2005) Photocatalytic water splitting with the Cr-doped $Ba_2In_2O_5/In_2O_3$ composite oxide semiconductors. Chem Mater 17:3255–3261
140. Yoshimura J, Ebina Y, Kondo J et al (1993) Visible-light induced photocatalytic behavior of a layered perovskite type niobate, $RbPb_2Nb_3O_{10}$. J Phys Chem 97:1970–1973
141. Hosogi Y, Shimodaira Y, Kato H et al (2008) Role of Sn^{2+} in the band structure of SnM_2O_6 and $Sn_2M_2O_7$ (M = Nb and Ta) and their photocatalytic properties. Chem Mater 20:1299–1307
142. Hosogi Y, Tanabe K, Kato H et al (2004) Energy structure and photocatalytic activity of niobates and tantalates containing Sn(||) with a $5s^2$ electron configuration. Chem Lett 33:28–29
143. Hosogi Y, Kato H, Kudo A (2006) Synthesis of $SnNb_2O_6$ nanoplates and their photocatalytic properties. Chem Lett 35:578–579
144. Kato H, Kobayashi H, Kudo A (2002) Role of Ag^+ in the band structures and photocatalytic properties of $AgMO_3$ (M: Ta and Nb) with the perovskite structure. J Phys Chem B 106:12441–12447

145. Hosogi Y, Kato H, Kudo A (2008) Photocatalytic activities of layered titanates and niobates ion-exchanged with sn^{2+} under visible light irradiation. J Phys Chem C 112:17678–17682
146. Ikeue K, Shiiba S, Machida M (2010) Novel visible-light-driven photocatalyst based on Mn-Cd-S for efficient H_2 evolution. Chem Mater 22:743–745
147. Zhang W, Xu R (2009) Surface engineered active photocatalysts without noble metals: CuS-$Zn_xCd_{1-x}S$ nanospheres by one-step synthesis. Int J Hydrogen Energ 34:8495–8503
148. Yan HJ, Yang JH, Ma GJ et al (2009) Visible-light-driven hydrogen production with extremely high quantum efficiency on Pt-PdS/CdS photocatalyst. J Catal 266:165–168
149. Li YX, Ma GF, Peng SQ et al (2009) Photocatalytic H_2 evolution over basic zincoxysulfide ($ZnS_{1-x-0.5y}O_x(OH)_{(y)}$) under visible light irradiation. Appl Catal A Gen 363:180–187
150. del Valle F, Ishikawa A, Domen K et al (2009) Influence of Zn concentration in the activity of $Cd_{1-x}Zn_xS$ solid solutions for water splitting under visible light. Catal Today 143:51–56
151. Zhang XH, Jing DW, Liu MC et al (2008) Efficient photocatalytic H_2 production under visible light irradiation over Ni doped $Cd_{1-x}Zn_xS$ microsphere photocatalysts. Catal Commun 9:1720–1724
152. Jang JS, Borse PH, Lee JS et al (2008) Indium induced band gap tailoring in $AgGa_{1-x}In_xS_2$ chalcopyrite structure for visible light photocatalysis. J Chem Phys 128:154717-1–154717-6
153. Zhang K, Jing DW, Xing CJ et al (2007) Significantly improved photocatalytic hydrogen production activity over $Cd_{1-x}Zn_xS$ photocatalysts prepared by a novel thermal sulfuration method. Int J Hydrogen Energ 32:4685–4691
154. Arai T, Senda SI, Sato Y et al (2008) Cu-doped ZnS hollow particle with high activity for hydrogen generation from alkaline sulfide solution under visible light. Chem Mater 20:1997–2000
155. Bao NZ, Shen LM, Takata T et al (2008) Self-templated synthesis of nanoporous CdS nanostructures for highly efficient photocatalytic hydrogen production under visible. Chem Mater 20:110–117
156. Chen D, Ye JH (2007) Photocatalytic H_2 evolution under visible light irradiation on $AgIn_5S_8$ photocatalyst. J Phys Chem Solids 68:2317–2320
157. Bang JH, Hehnich RJ, Suslick KS (2008) Nanostructured ZnS: Ni^{2+} photocatalysts prepared by ultrasonic spray pyrolysis. Adv Mater 20:2599–2603